# The Hydrodynamics and Energetics of Bioinspired Swimming with Undulatory Electromechanical Fins

Brittany Lynn Gater

Thesis submitted to the faculty of the Virginia Polytechnic Institute and State University in partial fulfillment of the requirements for the degree of

Masters of Science
In
Mechanical Engineering

Javid Bayandor
Steve Southward
Francine Battaglia

June 26, 2017
Blacksburg, Virginia, USA

Keywords: bioinspired robotics, swimming kinematics, undulatory locomotion, unsteady motion control, energy harvesting

# The Hydrodynamics and Energetics of Bioinspired Swimming with Undulatory Electromechanical Fins

Brittany Lynn Gater

## ACADEMIC ABSTRACT

Biological systems offer novel and efficient solutions to many engineering applications, including marine propulsion. It is of interest to determine how fish interact with the water around them, and how best to utilize the potential their methods offer. A stingray-like fin was chosen for analysis due to the maneuverability and versatility of stingrays.

The stingray fin was modeled in 2D as a sinusoidal wave with an amplitude increasing from zero at the leading edge to a maximum at the trailing edge. Using this model, a parametric study was performed to examine the effects of the fin on surrounding water in computational fluid dynamics (CFD) simulations. The results were analyzed both qualitatively, in terms of the pressure contours on the fin and vorticity in the trailing wake, and quantitatively, in terms of the resultant forces and the mechanical power requirements to actuate the desired fin motion. The average thrust was shown to depend primarily on the relationship between the swimming speed and the frequency and wavelength (which both are directly proportional to the wavespeed of the fin), although amplitude can be used to augment thrust production as well. However, acceleration was shown to significantly correlate with a large variation in lift and moment, as well as with greater power losses.

Using results from the parametric study, the potential for power regeneration was also examined. Relationships between frequency, velocity, drag, and power input were determined using nonlinear regression that explained more than 99.8% of the data. The actuator for a fin was modeled as a single DC motor-shaft system, allowing the combination of the energetic effects of the motor with the fin-fluid system. When combined, even a non-ideal fin model was able to regenerate more power at a given flow speed than was required to swim at the same speed. Even in a more realistic setting, this high proportion of regenerative power suggests that regeneration and energy harvesting could be both feasible and useful in a mission setting.

**The Hydrodynamics and Energetics of Bioinspired Swimming with Undulatory Electromechanical Fins**

Brittany Lynn Gater

## GENERAL AUDIENCE ABSTRACT

Animals interact with the world much differently than engineered systems, and can offer new and efficient ways to solve engineering problems, including underwater vehicles. To learn how to move an underwater vehicle in an environmentally conscious way, it is useful to study how a fish's movements affect the manner in which it moves through the water. Through careful study, the principles involved can be implemented for an efficient, low-disturbance underwater vehicle. The particular fish chosen for in-depth study was the stingray, due to its maneuverability and ability to travel close to the seafloor without disturbing the sediment and creatures around it.

In this work, computational analysis was performed on a model of a single stingray fin to determine how the motion of the fin affects the water around it, and how the water affects the fin in turn. The results were analyzed both in terms of the wake behind the fin and in terms of how much power was required to make the fin move in a particular way. The speed of the fin motion was found to have the strongest effect in controlling swimming speed, although the lateral motion of the fin also helped with accelerating faster.

Additionally, the potential for a robotic stingray fin to harness power from the water around it was examined. Based on results from simulations of the fin, a mathematical model was formulated to relate energy harvesting with the flow speed past the fin. This model was used to determine how worthwhile it was to use energy harvesting. Analysis of the model showed that harvesting energy from the water was quite efficient, and would likely be a worthwhile investment for an exploration mission.

**Acknowledgements**

I would first like to thank my advisor, Dr. Javid Bayandor, for the opportunity to work on this project. Working with you has been an honor and a privilege and I thank you for your guidance and direction. Thank you also to my committee members, Dr. Battaglia and Dr. Southward, for guidance and insight regarding CFD and controls, respectively. I would like to thank the previous researchers on this project, the senior design teams that kicked off the research in this area. A special thank you also goes to Cathy Hill, for her assistance in navigating the waters of graduate school paperwork, and to Diana Israel for her assistance with placing orders, purchasing equipment, and reserving rooms.

I would also like to thank my colleagues in the CRASH Lab, who have supported me through this journey. In particular, I would like to thank Jeffrey Feaster, both for teaching me the fundamentals of CFD and for encouraging and mentoring me throughout the process.

Finally, I would like to thank my friends and family for their love and support, particularly my fiancé, John Hutchinson. Thank you for being patient with me and supporting me through both my undergraduate and my graduate career and involvement in this work.

**Table of Contents**

**List of Figures**

**List of Tables**

**Foreword**

This thesis is written in manuscript format and contains two papers directly related to the Master's thesis. I am the first author on the included papers and was directly involved in all aspects of the contained work including simulation setup, validation, verification, post-processing, and analysis, in addition to the writing itself. The co-authors on the paper include my advisor and a colleague who helped set up the initial computational fluid dynamics simulations. Details of the work not discussed in the main body of the thesis, as well as revisions and other notes, can be found in the appendix.

## 1. Introduction

Mankind has long turned toward nature as an inspiration for invention. When combined with our current scientific understanding of the world and computational capabilities, the potential for understanding the way biological systems interact with the world and using those principles to design new ways of approaching engineering problems is enormous. This thesis will explore the capabilities of a bio-inspired underwater propulsive system in terms of its dynamics and power characteristics, and attempt to both explain aspects of the biological system and applications for robotics.

One of the best applications for an underwater bio-inspired propulsor is for exploration. Using fish-like fins would not only make a vehicle feel less intrusive to other fish, as observed in robotic experiments [1], it also provides the potential for drastically reducing local disturbances near the ocean floor, which could otherwise kick up too much sediment to take useful data or even destroy local wildlife. As such, let us consider bio-inspired propulsors in terms of niches most useful for exploration.

Fish morphology and movement varies drastically depending on niche. Typically, fish can be categorized by specialization for different movement types: namely, acceleration, cruising, and maneuverability [2]. This specialization is related to their particular niche, and does affect both morphology and the manner in which fish use their fins and body to propel themselves through the water. For exploring the seafloor, maneuverability is arguably the most useful of the three because it would allow finer precision of movement. As such, let's consider what characteristics fish in the "maneuverability" specialization tend to have. These fish tend to use median-paired fins (MPF) [3], which could either be short-based oscillatory fins or long-based undulatory fins. In this study, I opted for the long-based fin type, which also provide the opportunity to take advantage of kinematic capabilities of sprinters/cruisers. In particular, I chose to study the rajiform mode of locomotion, which uses long-based pectoral fins with undulatory motion, and is typically exhibited by batoids, fish of the superorder Batoidea, including rays and skates.

The fin motion of batoids are typically categorized by the number of waves, or wave number, present on their fins at a given time. If this value is greater than one, it is considered undulatory; if less than 0.5, it is oscillatory. Of course, the wave numbers of these fish fall along a spectrum, with higher wave numbers corresponding to rajiform locomotion while lower wave numbers correspond to mobuliform locomotion [4]. The wave number is correlated to the fin motion, morphology, and

the niche of the particular species, although not always in an obvious way. Typically, a lower wave number corresponds to pelagic rays, or those that live in the open ocean, which use lower frequency, higher amplitude flapping motions, and have longer, triangular shaped fins. Meanwhile, a higher wave number typically corresponds to benthic rays, or those that live near the seafloor, and typically use a higher frequency, lower amplitude fin motion, and have shorter, rounder fins.

To understand the fin kinematics of rajiform batoids better, consider the blue-spotted stingray *Taeniura lymma* (*T. lymma*) studied by Rosenberger [5] and the freshwater stingray *Potamotrygon orbignyi* (*P. orbignyi*) studied by Blevins and Lauder [6]. Rosenberger found that *T. lymma* demonstrated a strong correlation between propulsive wavespeed (how quickly the fin wave travels from anterior to posterior, and controlled with both wavelength and frequency) and swimming speed, with individuals showing different wave amplitudes but without significant modification in amplitude to adjust the swimming speed. Additionally, electromyographic (EMG) data showed that the fin motion was actuated by alternate firing of the dorsal and ventral muscles, with muscle activity in all parts of the fin from the anterior to the posterior. This result suggests that the fin wave is actively controlled, rather than passively, as the wave propagates from the front to the rear. Blevins, meanwhile, found that for *P. orbignyi*, the swimming speed was predominantly controlled by frequency, with constant parameters for wavelength and amplitude. Figure 1 shows an example of the wave along the stingray's fins during swimming in this experiment. This study also found that for *P. orbignyi*, the amplitude increased approximately linearly on a subset of the fin (from approximately 0.2 disc lengths from the front to about 0.7), and was approximately constant elsewhere.

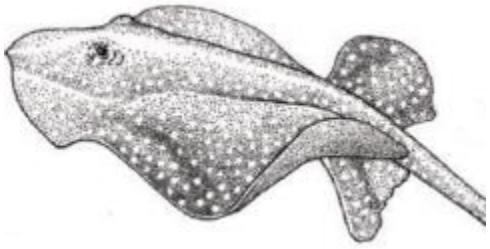

*Figure 1-1: A freshwater stingray swimming through the water by propagating an undulatory wave of increasing amplitude along the length of the fin.*

Next, let us turn toward the more general topic of what is known about the hydrodynamics and energetics involved for general fish swimming, as well as for batoids specifically. Researchers have approached this problem in a wide variety of ways over the years. The most widely-used

model for the propulsion of swimming fish is the elongated body theory (EBT) put forward by Lighthill [7]. The theory assumes inviscid flow over a slender fish with small amplitude tail movements, and determines approximate relationships between the kinematics of the fish and the resulting thrust, power, and efficiency. Although limited in scope, expansions have been made to the model to account for large amplitude [8] and added-mass terms [9] to make it significantly more general. The simple formula used for efficiency $\eta$ is:

$$\eta = \frac{1}{2}\left(1 + \frac{U}{V}\right) \tag{1}$$

where $U$ is the swimming speed and $V$ is the wavespeed of undulation, which assumes that a fish would keep the wave amplitude constant at the trailing edge. However, as shown by Cheng and Blickhan [10], efficiency calculated for fish with a variable amplitude at the tail could be as much as 20% lower than the true value. Additionally, the model of the forces still relies upon a coefficient of drag $c_D$ that would not only need to be experimentally determined for specific applications, but could also change depending on the motion of the fish body itself. To fill in the gaps of the model, much research has been done both experimentally and numerically to better understand the mechanics and hydrodynamics of fish locomotion.

One way in which the mechanics can be better understood is through study of the hydrodynamics of the wake, either through a flow visualization experiment or through CFD. As shown by Triantafyllou et al [11], a wake pattern behind an oscillating fin will produce a von Karman vortex street when in drag, and a reverse von Karman vortex street when in thrust. In other words, during each flap cycle, two vortices of opposing rotation are shed behind the tail, producing a wake with a propulsive jet if in net thrust, but a low pressure region if in net drag. For fish, the regime for which this wake produces optimal efficiency is typically associated with a Strouhal number

$$St = fA/U \tag{2}$$

in the range 0.25-0.35. As shown more recently by Eloy [12] using principles from EBT, the optimal Strouhal number is not limited to a strict interval, but rather shows a consistent trend with a dimensionless parameter termed the Lighthill number

$$Li = \frac{S}{h^2} C_d \tag{3}$$

where $S$ is the wetted surface area, $C_d$ is the drag coefficient, and $h$ is the height of the tail.

Although the reverse von Karman street is considered the classical representation of the wake, different wake patterns can also emerge. Depending on the kinematics and Reynolds number, one could also observe vortex dipoles [13], symmetry-breaking patterns [14], or double-row vortices [15], to name a few. In three dimensions, shed vortices can interlace in complex ways for both an oscillating fin [16] and an undulatory one [17], even for relatively simple fin structures. The particular wake that develops for a particular set of kinematics is likely based on the hydrodynamic wake resonance, as proposed by Moored et al based on eigenvalue analysis through vorticity perturbations in the wake [18]. This notion of a resonant frequency of the wake has also been experimentally supported through flow visualization with a flexible fin observed for several wake types [19].

The existence of multiple modes for a wake suggests that a control system may need to take fairly complex flow patterns into account. However, full numerical simulations of the fluid flow in an optimal controller require restrictively time-intensive computations [20]. Faster dynamic simulations are possible, as demonstrated by the eel-like robot of Porez et al [21]–[23]. However, designing higher performance controllers still requires a more general understanding of the underlying physics. By assuming sufficiently small or non-chaotic flow structures in the surrounding environment, a controller could also to focus on a single mode for optimization. Because steady swimming shows a balanced vortex street [14], with regular and reverse von Karman vortex streets obtained through perturbations of kinematic parameters and swimming speed, the classic vortex streets are the most likely to arise in a forward swimming context, rendering them the most useful for control analysis.

Parametric studies of the kinematics of undulation provide one of the best ways in which to understand the mechanics behind the vortex streets present in undulatory systems. The most comprehensive study of undulatory kinematics studied interactions between amplitude, wavespeed, wave number, and amplitude envelope on a 2D wavy plate [24]. Dong et al found that the net drag was approximately zero at a phase velocity $V/U$ of 1, suggesting that for an undulatory fin, steady swimming will tend to occur when the wavespeed is approximately equal to the swimming speed. Additionally, the root-mean-square (RMS) of the drag was minimized at $V/U$ = 1, and the RMS lift increased monotonically with wavespeed, suggesting that kinematics can be varied in such a way as to reduce the variation of forces, thereby reducing the motion of the center of mass (COM) of a vehicle. Amplitude variation at $V/U$ = 1.5 also showed that increasing

amplitude significantly increased the average thrust, but also increased the total power of the system, suggesting that there exists an amplitude which would yield the highest efficiency for the system. Similar results have also been observed in later works, even for 3D simulations [25–29].

Another fascinating result of Dong's study was the presence of a regime in which negative power input was observed, implying that the fin motion was driven by the flow and not the other way around. Although researchers frequently assess the efficiency of bioinspired flows, and regularly quantify the energetics involved, the majority of the work on efficiency focuses on the peaks of efficiency [11, 19, 26, 27, 30, 31]. However, the investigation of the region of negative power, in which the flow actuates the fin, shows potential for implementation of regenerative schemes. In an underwater environment, in which currents and flows are very common, a properly designed exploratory vehicle could consistently take advantage of power regeneration to improve its mission life indefinitely. To exploit this phenomenon, however, requires a prescribed waveform for a fixed long-based fin. Currently, most full-fledged undulatory robots use a series of servo motors to achieve a highly variable, controllable waveform, which would be unsuitable for regeneration from a fixed waveform. For regeneration, each fin would ideally be driven by a single motor, with the prescribed motion achieved either through a geared system [16] or a crankshaft. An example of such a single-motor undulatory system, developed by Clark and Smits is shown in Fig 1. The circuitry itself would require a DC motor, a rechargeable battery, and an H-bridge for the most effective implementation [32]. To the author's knowledge, no other studies on power regeneration for robotic applications in a bioinspired undulatory system have been investigated.

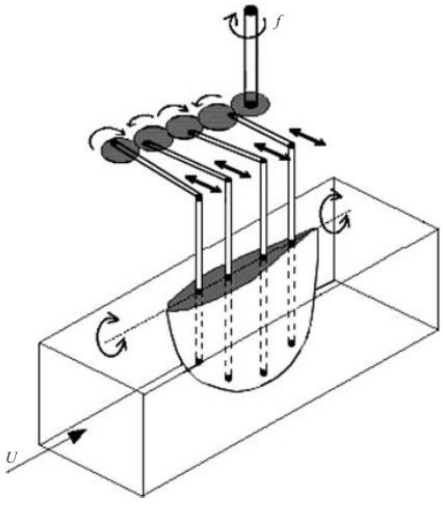


*Figure 1-2: An undulatory fin driven by a single motor using a gear train attached to stiff rods [16].*

The first manuscript in this thesis, in Section 2 [33], also uses a 2D wavy plate structure for a parametric study. However, the Reynolds number for this study ranged from $4 \times 10^4$ to $4 \times 10^5$, almost two orders of magnitude higher than the wavy plate experiment. Based on the suppression of separation and turbulence of fish even up to a Reynolds number of $10^7$ [34], a laminar model was used for simulation. The higher Reynolds number resulted in a relative decrease of friction forces, allowing the focus of the work to be on the inertial effects. Additionally, the leading edge of the waveform is fixed, which forces the fin to rely on the added-mass effect for thrust production with minimal augmentation from a leading edge vortex (LEV) [35]. In this way, the effects of the fin kinematics on the added-mass phenomenon can be separated from effects on LEV formation.

For the simulations, the fin location and deformation was prescribed, as was a constant, uniform flow parallel to the centerline of the fin. Because the fin motion was prescribed and the 2D cross-section chosen was along a midline of a 3D fin, the tail, which was outside of the range of the 2D cross-section, was not included in these simulations. The prescribed fin motion utilized a travelling wave with linearly increasing amplitude to approximate the midline of a stingray's fin motion. Although a stingray fin wave propagates radially along a disk, the cross-section chosen assumes linear propagation to represent the most likely scenario for implementation of a robotic fin. In a long-based robotic fin, actuation is commonly achieved through a linear, not radial, propagating wave due to its simplicity of implementation. Based on the analysis of Wu [34] in a review of fish swimming, the acceleration potential of the wake goes to zero at the edge of long-based fins, suggesting that the vorticity is bound to the side edge of a finite length fin and goes to zero at the trailing edge. As such, results of a 2D analysis of the wake can be used to develop a better understanding of the response of a 3D fin system. For the analysis, the kinematic parameters were varied individually around a steady swimming condition for the simulated fin to determine their effects on the resultant forces and energetics. The results are then interpreted in the context of robot design for exploration mission applications. For example, we have developed a prototype, shown in Figure 3, which could greatly benefit from the results of the parametric study in terms of its control development and implementation.

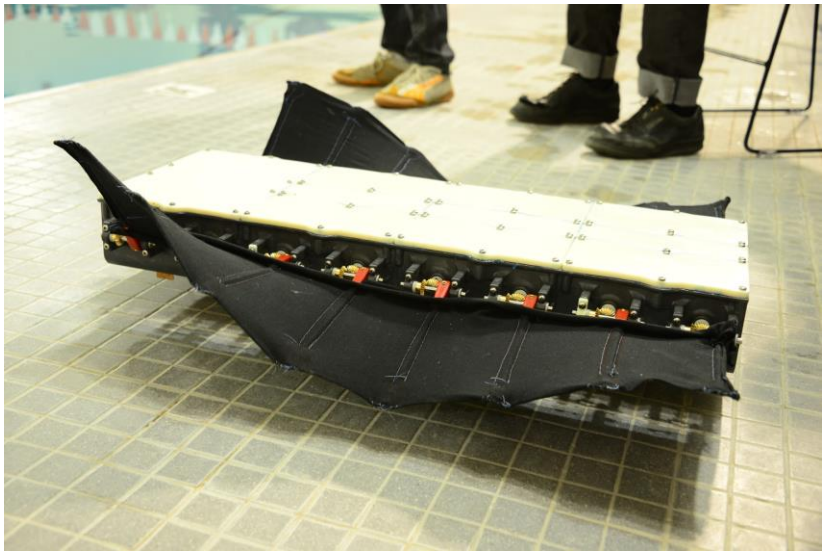

*Figure 1-3:A prototype of an undulatory robot developed by CRASH Lab designed to implement fin kinematics similar to those used in the CFD simulations of this manuscript.*

The second manuscript, in Section 3 [36], uses results from the Section 2 to design a parametric study into the interaction between frequency and velocity regarding drag and power characteristics. The objective of this study was to develop a methodology and a model for estimating the regenerative capacity of an undulatory fin in flow for a non-ideal system. By assuming the presence of a theoretical fin design using only a single motor for actuation, possibly using a gear train or crankshaft to prescribe the fin wave, the fluid model was combined with an electromechanical model for analysis. Using the resultant model, a case study is also used to demonstrate the effectiveness of a regenerative fin in a mission context. Ultimately, the goal of this thesis is to improve the understanding of undulatory fin dynamics for the purpose of designing an efficient robot and control strategy.


[1] M. M. D. M. Rahman, "Study on biomimetic squid-like underwater robots with two undulating side fins," phdthesis, Osaka University, 2013.

[2] P. W. Webb, "Form and Function in Fish Swimming," *Sci. Am.*, vol. 251, no. 1, pp. 72–82, 1984.

[3] M. Sfakiotakis, D. M. Lane, and J. B. C. Davies, "Review of fish swimming modes for aquatic locomotion," *IEEE J. Ocean. Eng.*, vol. 24, no. 2, pp. 237–252, 1999.

[4] L. J. Rosenberger, "Pectoral fin locomotion in batoid fishes: undulation versus oscillation.," *J. Exp. Biol.*, vol. 204, no. Pt 2, pp. 379–394, 2001.

[5] L. J. Rosenberger and M. Westneat, “Functional morphology of undulatory pectoral fin locomotion in the stingray taeniura lymma (Chondrichthyes: dasyatidae),” *J. Exp. Biol.*, vol. 202 Pt 24, pp. 3523–39, 1999.

[6] E. Blevins and G. V. Lauder, “Rajiform locomotion: three-dimensional kinematics of the pectoral fin surface during swimming in the freshwater stingray Potamotrygon orbignyi,” *J. Exp. Biol.*, vol. 215, no. 18, pp. 3231–3241, 2012.

[7] M. J. Lighthill, “Note on the swimming of slender fish,” *J. Fluid Mech.*, vol. 9, no. 2, p. 305, 1960.

[8] M. J. Lighthill, “Large-amplitude elongated-body theory of fish locomotion,” *Proc. R. Soc. Lond. B.*, vol. 179, pp. 125–138, 1971.

[9] M. J. Lighthill, “Aquatic animal propulsion of high hydromechanical efficiency,” *J. Fluid Mech.*, vol. 44, no. 2, p. 265, 1970.

[10] J. Cheng and R. Blickhan, “Note on the Calculation of Propeller Efficiency Using Elongated Body Theory,” *J. Exp. Biol.*, vol. 192, pp. 169–77, 1994.

[11] G. S. Triantafyllou, M. S. Triantafyllou, and M. A. Grosenbaugh, “Optimal thrust development in oscillating foils with application to fish propulsion,” *Journal of Fluids and Structures*, vol. 7, no. 2. pp. 205–224, 1993.

[12] C. Eloy, “Optimal Strouhal number for swimming animals,” *J. Fluids Struct.*, vol. 30, no. 1, pp. 205–218, 2012.

[13] G. Y. He, S. G. Zhang, and X. Zhang, “Thrust generation and wake structure of wiggling hydrofoil,” *Appl. Math. Mech. (English Ed.*, vol. 31, no. 5, pp. 585–592, 2010.

[14] G. Y. He, Q. Wang, X. Zhang, and S. G. Zhang, “Numerical analysis on transitions and symmetry-breaking in the wake of a flapping foil,” *Acta Mech. Sin. Xuebao*, vol. 28, pp. 1–6, 2012.

[15] I. Borazjani and F. Sotiropoulos, “Numerical investigation of the hydrodynamics of anguilliform swimming in the transitional and inertial flow regimes.,” *J. Exp. Biol.*, vol. 212, no. Pt 4, pp. 576–592, 2008.

[16] R. P. Clark and A. J. Smits, “Thrust production and wake structure of a batoid-inspired oscillating fin,” *J. Fluid Mech.*, vol. 562, p. 415, 2006.

[17] I. D. Neveln, R. Bale, A. P. S. Bhalla, O. M. Curet, N. A. Patankar, and M. A. MacIver, “Undulating fins produce off-axis thrust and flow structures,” *J. Exp. Biol.*, vol. 217, no. Pt 2, pp. 201–213, 2014.

[18] K. W. Moored, P. a. Dewey, a. J. Smits, and H. Haj-Hariri, “Hydrodynamic wake resonance as an underlying principle of efficient unsteady propulsion,” *J. Fluid Mech.*, vol. 708, no. February 2015, pp. 329–348, 2012.

[19] D. B. Quinn, G. V. Lauder, and A. J. Smits, “Maximizing the efficiency of a flexible propulsor using experimental optimization,” *J. Fluid Mech.*, vol. 767, pp. 430–448, 2015.

[20] J. E. Colgate and K. M. Lynch, “Mechanics and control of swimming: A review,” *IEEE J.*

*Ocean. Eng.*, vol. 29, no. 3, pp. 660–673, 2004.

[21] F. Boyer, M. Porez, A. Leroyer, and M. Visonneau, "Fast Dynamics of an Eel-Like Robot - Comparisons With Navier - Stokes Simulations," *IEEE Trans. Robot.*, vol. 24, no. 6, pp. 1274–1288, 2008.

[22] M. Porez, V. Lebastard, A. J. Ijspeert, and F. Boyer, "Multi-physics model of an electric fish-like robot: Numerical aspects and application to obstacle avoidance," *IEEE Int. Conf. Intell. Robot. Syst.*, pp. 1901–1906, 2011.

[23] M. Porez, F. Boyer, and A. J. Ijspeert, "Improved Lighthill fish swimming model for bio-inspired robots: Modeling, computational aspects and experimental comparisons," *Int. J. Rob. Res.*, vol. 33, no. 10, pp. 1322–1341, 2014.

[24] G. J. Dong and X. Y. Lu, "Numerical analysis on the propulsive performance and vortex shedding of fish-like travelling wavy plate," *Int. J. Numer. Methods Fluids*, vol. 48, no. 12, pp. 1351–1373, 2005.

[25] Y. Zhang, J. Laibin, J. H. He, J. Yang, S. Zhang, and K. H. Low, "A numerical analysis of an undulatory mechanical fin driven by Shape Memory Alloy," *2006 IEEE Int. Conf. Robot. Biomimetics, ROBIO 2006*, vol. 4, pp. 73–78, 2006.

[26] J. Deng, X. M. Shao, and A. L. Ren, "Numerical study on propulsive performance of fish-like swimming foils," *J. Hydrodyn.*, vol. 18, no. 6, pp. 681–687, 2006.

[27] C. ZHANG, L.-X. ZHUANG, and X.-Y. LU, "Analysis of hydrodynamics for two-dimensional flow around waving plates," *J. Hydrodyn. Ser. B*, vol. 19, no. 1, pp. 18–22, 2007.

[28] H. Zhou, T. Hu, H. Xie, D. Zhang, and L. Shen, "Computational Hydrodynamics and Statistical Modeling on Biologically Inspired Undulating Robotic Fins: A Two-Dimensional Study," *J. Bionic Eng.*, vol. 7, no. 1, pp. 66–76, 2010.

[29] M. M. Rahman, Y. Toda, and H. Miki, "Computational Study on a Squid-Like Underwater Robot with Two Undulating Side Fins," *J. Bionic Eng.*, vol. 8, no. 1, pp. 25–32, 2011.

[30] J. M. Anderson, K. Streitlien, D. S. Barrett, and M. S. Triantafyllou, "Oscillating foils of high propulsive efficiency," *J. Fluid Mech*, vol. 360, pp. 41–72, 1998.

[31] L. Wen, T. Wang, G. Wu, and J. Liang, "Quantitative thrust efficiency of a self-propulsive robotic fish: Experimental method and hydrodynamic investigation," *IEEE/ASME Trans. Mechatronics*, vol. 18, no. 3, pp. 1027–1038, 2013.

[32] T. A. Haskew and E. M. Hill, "Regeneration mechanisms in a DC motor with an H-bridge inverter," *IEEE Int. Electr. Mach. Drives Conf. IEMDC 1999 - Proc.*, pp. 531–533, 1999.

[33] B. Gater, J. Feaster, F. Battaglia, and J. Bayandor, "Dynamics and propulsive efficiency of bio-inspired undulatory marine locomotion," in *ASME 2016 Fluids Engineering Division Summer Meeting*, 2016.

[34] T. Y. Wu, "A Review on Fish Swimming and Bird/Insect Flight," *Ann Rev Fluid Mech*, vol. 43, pp. 25–58, 2011.

[35] R. G. Bottom, I. Borazjani, E. L. Blevins, and G. V Lauder, “Hydrodynamics of swimming in stingrays : numerical simulations and the role of the leading-edge vortex,” *J. Fluid Mech.*, vol. 788, pp. 407–443, 2016.

[36] B. Gater and J. Bayandor, “Power Regeneration of a Bioinspired Electromechanical Propulsive Fin,” in *ASME 2017 Fluids Engineering Division Summer Meeting*, 2017.

## 2. Paper #1: Dynamics and Propulsive Efficiency of Bio-Inspired Undulatory Marine Locomotion

### 2.1. Abstract

*Computational fluid dynamics (CFD) was used to investigate the fluid mechanics for undulatory stingray locomotion. This method of undulatory propulsion can be utilized to generate non-turbulent thrust with minimal disturbance to the immediate environment, ideal for exploratory vehicles for underwater environments. Undulatory locomotion was modeled as a two-dimensional fin in free flow with a deforming non-slip boundary to represent a propagating sinusoidal wave with a linearly increasing amplitude, constant frequency, wavelength and flow velocity. In the presented computational study, we varied the amplitude, wavelength, frequency, and flow velocity parametrically and examined the effect on thrust, lift, and pitching moment. Average net thrust was found to increase with wavelength and frequency, whereas for this two-dimensional case amplitude showed negligible effects. For the parametric cases, a theoretical efficiency for forward propulsion was then calculated for a continuous fin. The amplitude was found to increase the input power required for actuation, but decreased output power for forward thrust. Variation of the other parameters showed that the output power depends nearly linearly on the input power, regardless of the particular kinematics or swimming speed.*

### 2.2. Introduction and Motivation

Recent technological advancements in computing and control methods have facilitated the development and feasibility of robotic vehicles for exploratory purposes. While many advances have been made to the field of ocean engineering, the need for more efficient propulsion to allow for longer dives necessitates research into alternative mechanisms. In response to this need, research has begun to turn to aquatic life for inspiration. These animals have evolved over millions of years to best navigate their prospective aquatic environments. In general, fish morphology directly relates to the specialization toward cruising, acceleration, and maneuverability [1]. Perhaps the most challenging of these is maneuverability, which in fish morphology corresponds to the undulation of long-based fins. One of the solutions to this issue of maneuverability present

in nature is batoid locomotion, which utilizes two large fins leveraging undulating waves passing from the anterior to the posterior of the animal [2].

Batoids typically move by propagating sinusoidal waves along the length of their fin, but the amplitude, frequency, and wave number vary depending on the species [2]. Analytical models have been developed to approximate the effect of these parameters on swimming dynamics, as in Lighthill's elongated body theory applied to balistiform and gymnotiform locomotion [3]. Additionally, studies of the vortical shedding from swimming suggest an optimal range of kinematics for particular swimming speeds corresponding to a Strouhal number between 0.2 and 0.4 [4] However, the particulars of undulatory batoid locomotion are still under investigation. The biological kinematics for Taeniura lymma and Potamotrygon orbignyi have been particularly investigated [5,6], lending some insight into the parameters used by these species. Of special note is the amplitude envelope found by Blevins and Lauder [6], which increased along the length of a portion of the fin.

The most common approach to understanding undulatory locomotion is to design and build a robotic system approximating one or two fins. Typically, these fins are mechanically discretized with a finite number of oscillating rods supporting transverse motion of the fin [7-14] Visualization of the flow has been done with particle image velocimetry (PIV), which can show the vortical shedding and amplitude of the resulting von Karman wake structure [15,16]. Another approach is to numerically solve the flow with computational fluid dynamics (CFD) for a continuous fin, typically with approximately constant amplitude along the length of the fin [17-20].

The previous study by Sharp et al [21] used CFD to investigate the effect of inlet speed on thrust production for a given set of kinematic parameters. The net thrust tended to vary nearly linearly with inlet velocity, with the thrust and drag balancing out around 0.76 m/s. Expanding on those results, Gater et al [22] discussed the general trends associated with each of the kinematic parameters in an initial parametric study.

This study focuses on using two-dimensional computational fluid dynamics to model the locomotion of a continuous robotic batoid fin during various kinematic motions and velocities. The amplitude envelope is approximated as linearly increasing along the entire length of the fin. The effect of kinematic parameters on the resulting forces and moments was investigated for the two-dimensional case. Using the force distributions, power characteristics for the system were also quantified and examined.

## 2.3. Theory and Procedure

### *2.3.1. Numeric Methodology*

The velocity and pressure fields around a dynamic two-dimensional cross-section of a fin are solved using the commercial software ANSYS Fluent (v. 15). Assuming an unsteady, incompressible flow, the continuity equation is:

$$\nabla \cdot \vec{v} = 0 \tag{1}$$

where $\vec{v}$ is the velocity vector. Neglecting gravitational effects, the incompressible unsteady momentum equation is:

$$\rho \left[\frac{\partial \vec{v}}{\partial t} + \vec{v} \cdot (\nabla \vec{v})\right] = -\nabla p + \nabla \cdot \bar{\bar{\tau}}$$

where $\rho$ is the fluid density, $t$ is time, $p$ is the pressure, and $\bar{\bar{\tau}}$ is the fluid stress tensor.

The presented incompressible flow is solved using the segregated pressure-based Navier-Stokes (PBNS) solver [23] with the semi-implicit method for pressure linked equations (SIMPLE) algorithm used to resolve pressure-velocity coupling. The gradients are discretized using the least squares cell based (LSCB) method. The momentum equations are discretized using the second-order upwind scheme and time is discretized using a first-order implicit method. The absolute convergence criteria are set to $10^{-7}$ for continuity, U and V. The time step was determined using the Courant-Fredrichs-Levy (CFL) number:

$$CFL = \frac{U_\infty \Delta t}{\Delta x} \tag{3}$$

where $\Delta t$ is the time step and $\Delta x$ is the smallest cell size. For all simulations, the CFL was less than one, with a maximum of 0.90 and a minimum of 0.13. Additionally, the Reynolds number varied between $4 \times 10^4$ and $4 \times 10^5$ for all cases. Because the Reynolds number remained less than the critical Reynolds number and the solution converged for all cases, no turbulence model was implemented.

An unstructured finite-volume mesh is generated around the cross-section and is updated with each time step to retain simulation accuracy at all times, using a combination of diffusive smoothing and domain remeshing functions. At the beginning of each time step the diffusion function is applied first, with the remeshing function occurring directly afterwards to correct for extreme mesh deformation. The diffusive smoothing is defined as

$$\nabla \cdot \left(\gamma \nabla \vec{\psi}\right) = 0 \tag{4}$$

where the diffusion coefficient $\gamma$ defines the degree to which the boundary motion $\vec{\psi}$ propagates through the surrounding fluid mesh. $\gamma$ is calculated using the cell distance from the deforming boundary $d$.

$$\gamma = \frac{1}{d^a} \tag{5}$$

Solving Eq. 4 for $\vec{\psi}$, the mesh distribution at the next time step $\vec{x}_{t+1}$ is solved using $\vec{\psi}$, $\Delta t$ and the present mesh distribution $\vec{x}_t$.

$$\vec{x}_{t+1} = \vec{x}_t + \vec{\psi}\,\Delta t \tag{6}$$

The diffusion parameter was set to $a=$1.75 for this study.

A remeshing function is implemented to resolve the extreme boundary motions present in undulatory locomotion. A secondary mesh is used to retain the consistency of the fluid data during remeshing. The remeshing function uses the nodal distance from the nearest boundary $d_{min}$ and the most remote node from the boundaries $d_{max}$ to normalize the boundary distance $d_b$:

$$d_b = \frac{d_{min}}{d_{max}} \tag{7}$$

$d_b$ is then used to determine the cell size at the location of interest $size_i$

$$size_i = size_b \times \Gamma \tag{8}$$

where $\Gamma$ is the sizing function factor, defined by the size function variation $\alpha$ and the size function rate $\beta$. Two different equations for $\Gamma$ are implemented depending upon the sign of $\alpha$:

$$\begin{aligned} \Gamma &= 1 + a d_b^{1+2\beta} \quad , \quad \alpha > 0 \\ \Gamma &= 1 + a d_b^{\frac{1}{1-\beta}} \quad , \quad \alpha < 0 \end{aligned} \tag{9}$$

Combining Eq. 8, 9 yields the allowable size of a cell in the fluid volume. Using the remeshing functions with diffusion smoothing yields a robust, highly refined mesh as can be seen in Fig. 1. The parameters used in this study were $\alpha = 1.1$ and $\beta = 0.15$. Figure 1 shows the unstructured 2D mesh immediately surrounding the fin cross-section after 7s of simulation.

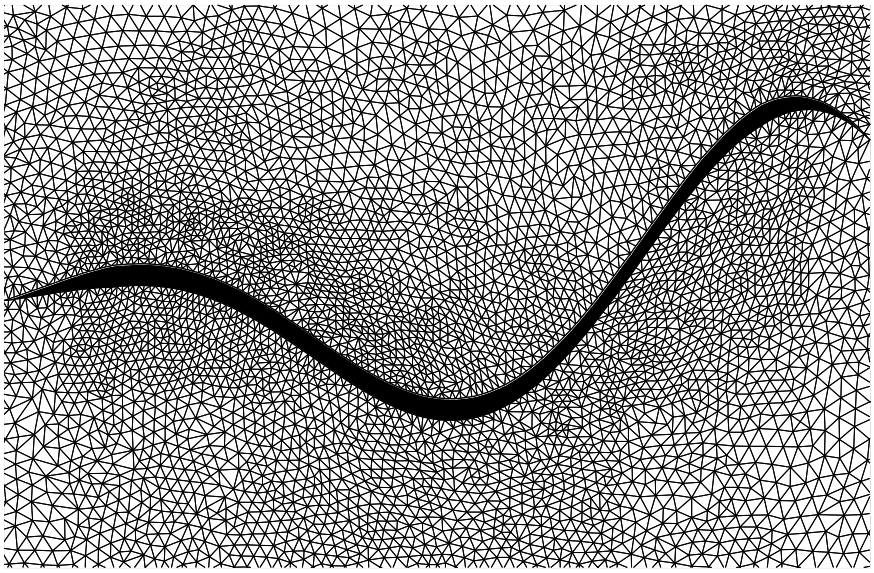

*Figure 2-1: The unstructured triangular mesh used in the domain around the fin.*

Using the aforementioned computational methods, the forces acting on an element along the fin surface $F_i$ are calculated using $p$ and $\bar{\bar{\tau}}$

$$\vec{F_i} = (\nabla p_i + \nabla \cdot \bar{\bar{\tau}}_i)(Area) \tag{10}$$

### *2.3.2. Computational Domain and Cases*

Water uniformly enters the computational domain along the left boundary with a specified uniform velocity $U_\infty$. The upper and lower boundaries of the fluid domain use a slip condition with the right side set at ambient pressure. It should be noted that the entire domain is 1.2m × 0.8m.

The fin is modeled in two dimensions using the cross section of a batoid fin. To approximate the amplitude envelope for the kinematics determined by Blevins and Lauder [6], the centerline of the motion is modeled by a sine wave with linearly increasing amplitude propagating across the fin, given by

$$y(x,t) = Ax \sin\left(\frac{2\pi}{\lambda}x - \omega t\right) \tag{11}$$

and shown graphically in Fig. 2. $y(x,t)$ is the vertical coordinate at a particular point in the geometry, $A$ is the slope of the amplitude of the propagating wave, $\lambda$ is the wavelength, $\omega$ is the angular frequency, $x$ is a spatial coordinate whose origin is at the front of the fin and increases rightward, and $t$ is time. The fin is 0.4m in length, with a constant vertical thickness of 0.01m and linear tapering of the thickness in the anterior and posterior 0.05m.

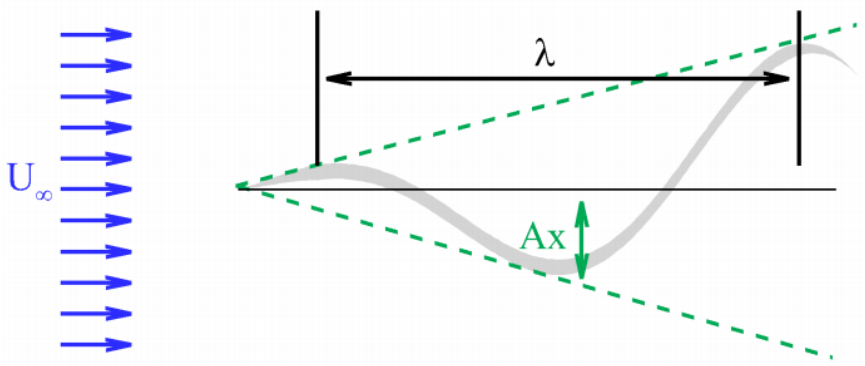


*Figure 2-2: The spatial parameters varied in the parametric study. A, λ, and $U_\infty$ are shown in relation to the fin.*

The cases run in the analysis are broken up into two parts: variations of $U_\infty$ for a given set of kinematic parameters to determine the net zero $F_x$ and parametric variation of kinematics for the $U_\infty$ previously defined. The velocity variation cases use kinematics of $\lambda = 0.335$ m, $\omega = 15$ rad/s, and $A = 0.25$. The fin frequency and wave number ($L/\lambda = 1.2$) were chosen to fit the range of the kinematics of the freshwater stingray Taeniura lymma investigated by Rosenberger [5]. The amplitude envelope slope was based on the region of increasing amplitude of the freshwater stingray Potamotrygon orbignyi, which showed approximately 1.5 cm amplitude developed over approximately 6 cm lengthwise, giving an amplitude slope of approximately 0.25 [6]. Based upon the $U_\infty$ variation cases, the net 0 $F_x$ was determined to be approximately 0.7625 m/s. This velocity was used for $U_\infty$ for the other cases, which were each varied individually while keeping other parameters at their aforementioned values.

### *2.3.3. Derivation of Power*

In general, the forces acting on the fluid from the body can be split into two categories: actuation and reaction. The actuation and reaction forces of a differential element of the body to the fluid can be quantified as follows, based on Newton's second law.

$$m\,\ddot{\vec{x}} = \Sigma\left(\vec{f}_{fluid} + \vec{f}_{fin} + \vec{f}_r\right) \tag{12}$$

For the purposes of this this study, the characteristic of interest is the power imparted to the fluid. Additionally, the fin inertia depends heavily on the mechanical design of the system in question. As such, fin inertia was neglected in favor of examining an ideal system for its effect directly on the fluid. This results in the following.

$$\vec{f}_{in} + \vec{f}_r = -\sum \vec{f}_{fluid} \tag{13}$$

However, because power is only consumed by inducing actuation forces (not reactionary ones), we will consider only the actuation force, which is acting in a direction defined by the unit vector $\vec{a}$. We will also assume that because the body of a physical system in the fluid would be unfixed relative to the reference frame, the actuation forces can account for all forces in the actuation direction, while the reaction forces result only from fluid forces that cannot be counteracted by actuation. This would cause the reaction forces to act in a direction orthogonal to the actuation force. As such, our equation reduces to

$$\vec{f}_{in} = \left[\left(-\sum \vec{f}_{fluid}\right) \cdot \vec{a}\right]\vec{a} \tag{14}$$

Now with this definition for actuation force, we can determine the power required for this actuation. In general, power consumption can be measured based on the rate of change of work into the system. Mechanical work into the fluid from the differential element can be quantified as the actuation forces acting over a distance in the same direction, as in the equation for differential work.

$$\partial w_{in} = \vec{f}_{in} \cdot d\vec{x} \tag{15}$$

To measure the power characteristics, the work equation is then differentiated with respect to time, resulting in the following.

$$\dot{w}_{in} = \vec{f}_{in} \cdot \vec{v} \tag{16}$$

Lastly, to measure the total power required to actuate the whole fin, we integrate the power for the differential element over the length of the fin.

$$\dot{W}_{in} = \int_0^L \vec{f}_{in}(s) \cdot \vec{v}(s) ds \tag{17}$$

For typical robotic implementations of undulatory fins, the fin is actuated using several rotary motors which rotate about the longitudinal axis of the fin base. In two-dimensions, this would result in actuation that only acts transverse to the fin (in the y-direction). As such, for this study, the direction of actuation force $\vec{a}$ was defined accordingly.

In addition to power consumption, it is also useful to determine a measure for output power. This is done in a similar manner to the input power, but considers the whole-body velocity response rather than that of a differential element. As such, we will first find the net force on the body in the desired direction denoted by unit vector $\vec{b}$ as follows, again neglecting inertia.

$$\vec{f}_{out} = \left[\left(-\sum \vec{f}_{fluid}\right) \cdot \vec{b}\right]\vec{b} \tag{18}$$

$$\vec{F}_{out} = \int_0^L \vec{f}_{out}(s)ds \tag{19}$$

Then, differentiating output work with respect to time results in the following.

$$\dot{W}_{out} = \vec{F}_{out} \cdot \vec{v} \tag{20}$$

Note that for our computational setup, the velocity of the body relative to the fluid is equal and opposite to the prescribed inlet velocity of the fluid to the computational domain, resulting in our final power output equation.

$$\dot{W}_{out} = -\vec{F}_{out} \cdot \vec{U}_{\infty} \tag{21}$$

## 2.4. Results and Discussion

### *2.4.1. Forces and Moments*

For the kinematics considered in this study, the expected and desired output is a net horizontal force. To develop a better understanding of how the kinematics affect this horizontal force, the time-averaged horizontal force was investigated for various parameter levels, as shown in Figure 3. Based on these results, this average horizontal force varies approximately linearly for both inlet velocity (swimming speed) and wavelength, with greater forward thrust for lower speeds and larger wavelengths. This average force also increases quadratically with frequency on this interval. Changes in amplitude, however, show negligible effects on the output force, suggesting that either amplitude does not significantly affect thrust on the interval studied[1], or that any effects from amplitude will occur primarily due to three-dimensional effects.

[1] Further research showed that this finding was a result of the interval studied. Further discussion of the amplitude effects can be found in Appendix C.

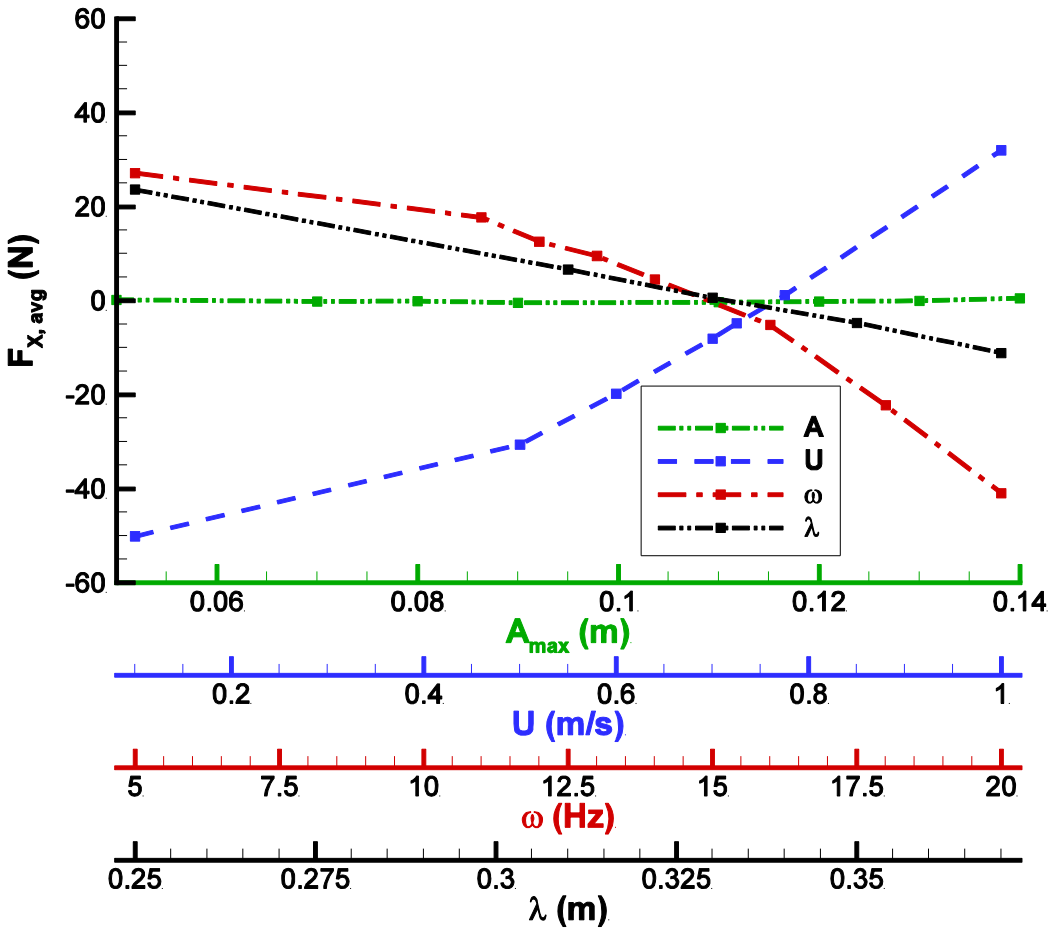


*Figure 2-3: Effect A, $U_\infty$, ω, and λ have on average $F_x$. Positive values indicate net drag; negative values, net thrust.*

For the purposes of this paper, the point at which these cases results in zero average horizontal force corresponds to the "steady-state" case. For a swimming body using this type of undulatory locomotion, this steady-state case would correspond to the average swimming velocity for the given set of kinematic parameters. This is not to say that the forces or velocities would not change at all for the swimming system, only that the average velocity would remain constant. The forces at this average velocity will vary sinusoidally at the frequency of vortex shedding, or twice the wave frequency of the fin.

Although thrust and drag are the primary forces of interest, it is also important to investigate the net lift and moments acting on the fin for the purposes of stability and control. The average lift forces for each case are shown in Figure 4, with the same force scale as for the drag case of Figure 3. The relatively low values for average lift suggest that these average vertical forces are negligible

relative to the horizontal ones. However, the average moments, shown in Figure 5, are not negligible. Although the pitching moment is small or close to zero near steady-state, there are significant non-random trends for the variation of moment with each kinematic parameter. This suggests that the pitching moment is significant, and should be accounted for when designing relevant control systems for stability.

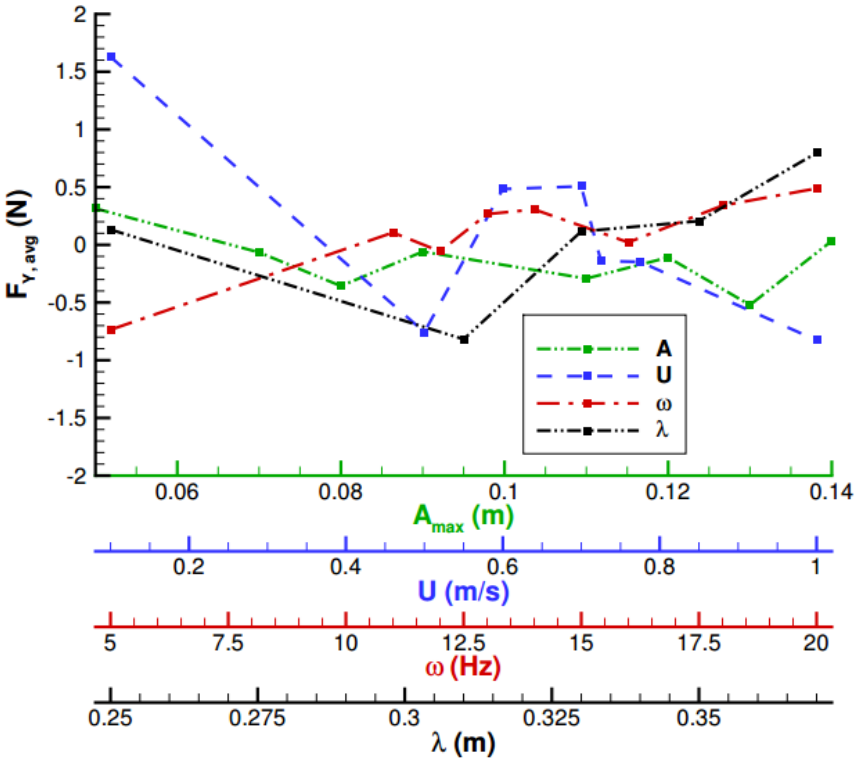


*Figure 2-4: Effect A, $U_\infty$, ω, and λ have on average $F_y$.*

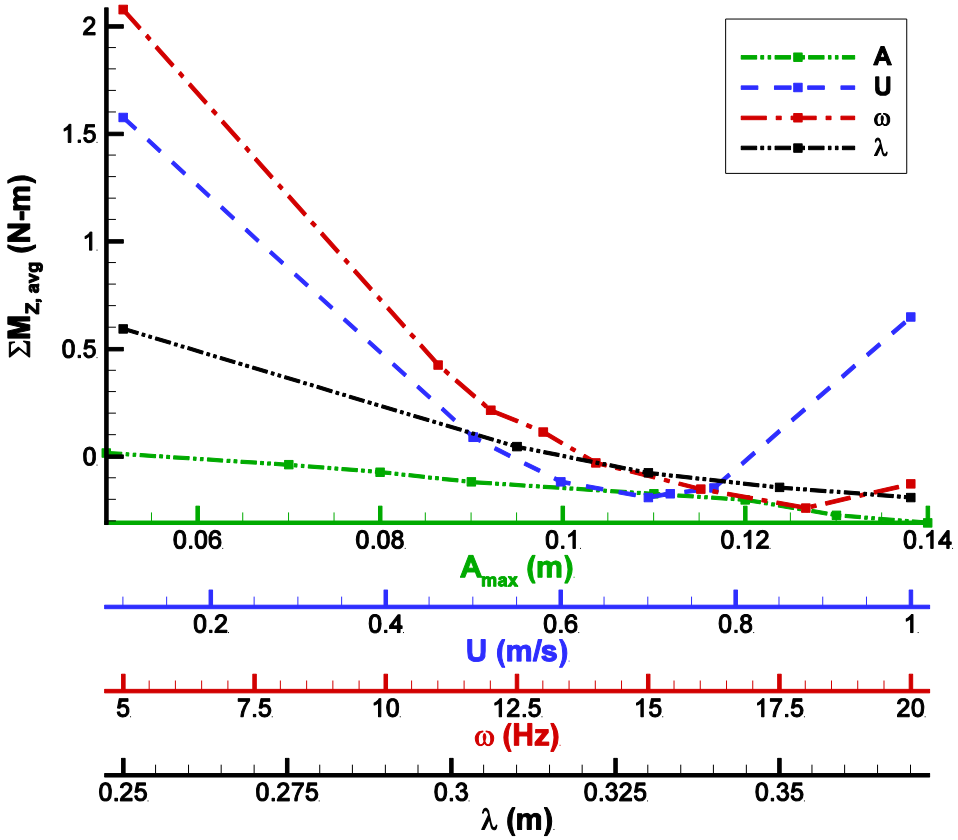


*Figure 2-5: Effect A, $U_\infty$, $\omega$, and $\lambda$ have on average $M_z$.*[2]

As mentioned previously, the forces present on the fin will vary periodically, meaning that the variance of forces should also be considered for analysis. This variance, for both forces and moments, was measured as the root-mean-square (RMS) value about the average. Note that for a sinusoidal signal, this will correspond to about 70.7% of the amplitude of the sinusoid.

The horizontal RMS forces, as shown in Figure 6, tend to be small, particularly near the steady-state case. For higher magnitudes of average horizontal forces, the RMS forces do also tend to be higher, but are still small relative to the average values. However, the RMS lift forces, as shown in Figure 7, are consistently large relative to the average drag values. For a large planform area, the hydrostatic pressure on the planform would tend to reduce the effect of these forces on the overall body motion, but are still important design considerations for systems intending to use this type of locomotion. Lastly, the RMS moment, shown in Figure 8, also tends to be large relative to the average pitching moment. As with the RMS lift, the effect of this variance on the body motion

[2] This is actually the average moment acting on the top side of the fin only; it is balanced out by the bottom side of the fin. The full average moment acting on the fin is much closer to 0.

would likely be reduced by a large planform area. Nevertheless, the varying pitching moments could be an important consideration for vehicle design or control system design.

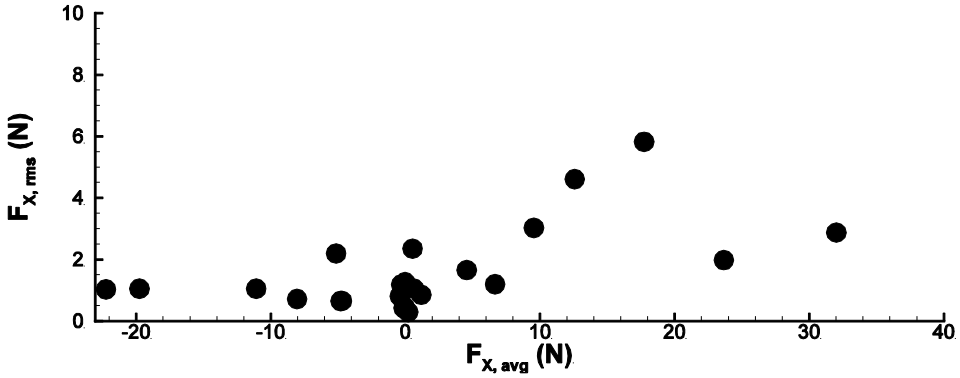


*Figure 2-6: Comparison of $F_{X,Avg}$ and $F_{X,RMS}$.*

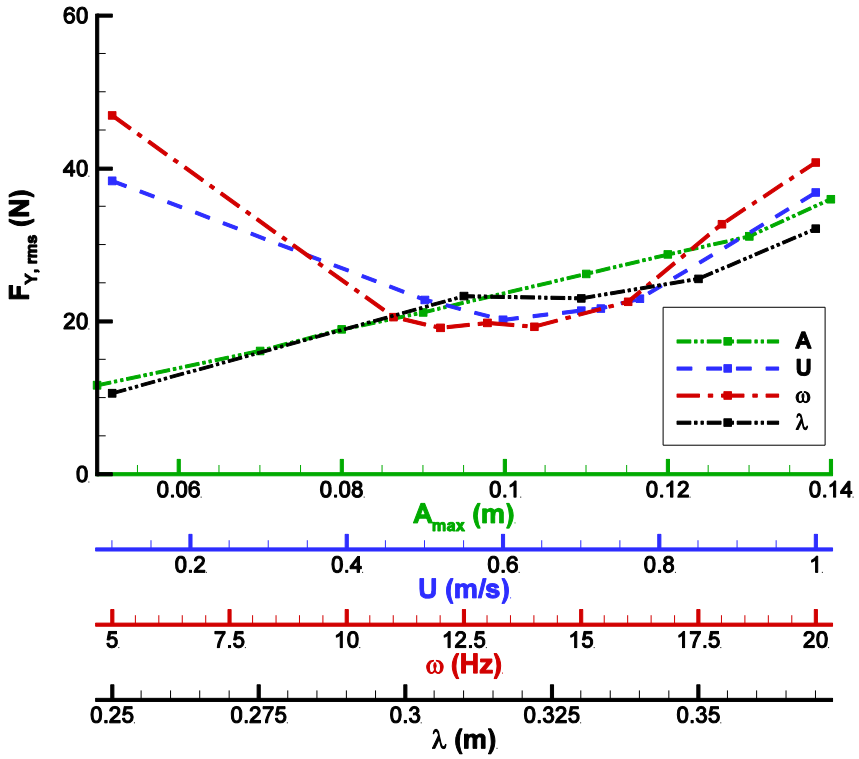


*Figure 2-7: Effect A, $U_\infty$, ω, and λ have on $F_{Y,RMS}$.*

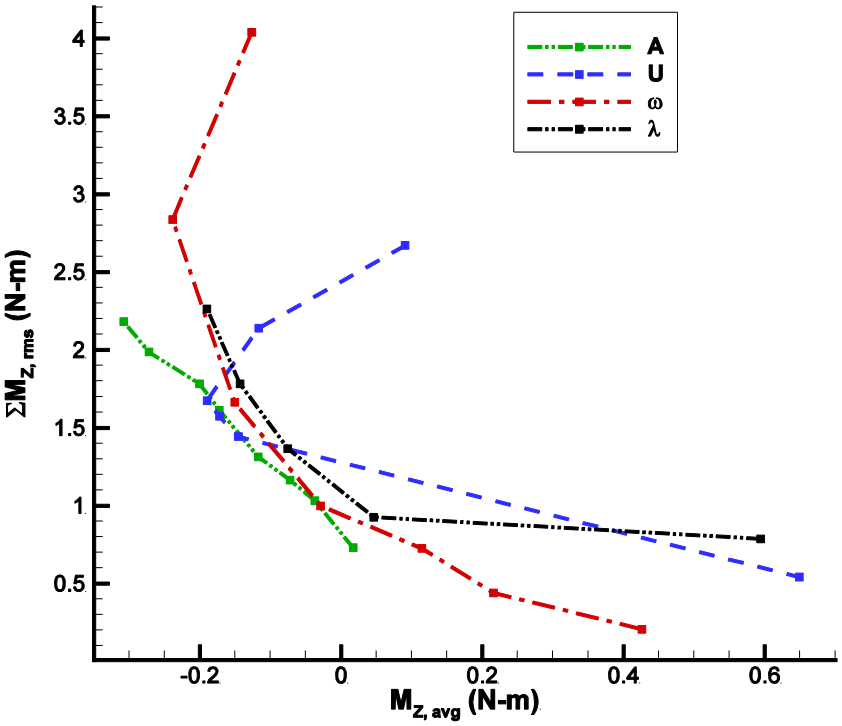


*Figure 2-8: Effect A, $U_\infty$, $\omega$, and $\lambda$ have on the pitching moment characteristics $M_{Z,RMS}$ vs $M_{Z,Avg}$.*

### *2.4.2. Power and Efficiency*

Now that we have a general understanding of the forces and moments acting on the system, the next step is to determine the optimal performance range in terms of power and efficiency. These power characteristics can provide insight into the design of both the mechanical and control systems. Meanwhile, the efficiency characteristics can provide a baseline model for comparison with other types of propulsion, including both typical engineering solutions and bio-inspired ones.

Using the methods discussed in the previous section, we calculated input and output power for a variety of cases to determine the parametric relationships between power and kinematic characteristics. Figure 9 shows these relationships for input power and each of the defined parameters. On the intervals investigated, we found that frequency and velocity each have approximately quadratic relationships with power. The wavelength and amplitude, meanwhile,

each appear to be directly proportional to power on this interval. One major point of note here is that for certain parametric values, it is possible to achieve a negative value for input power. Essentially, this means that it is possible to recover power from the surrounding fluid during motion.

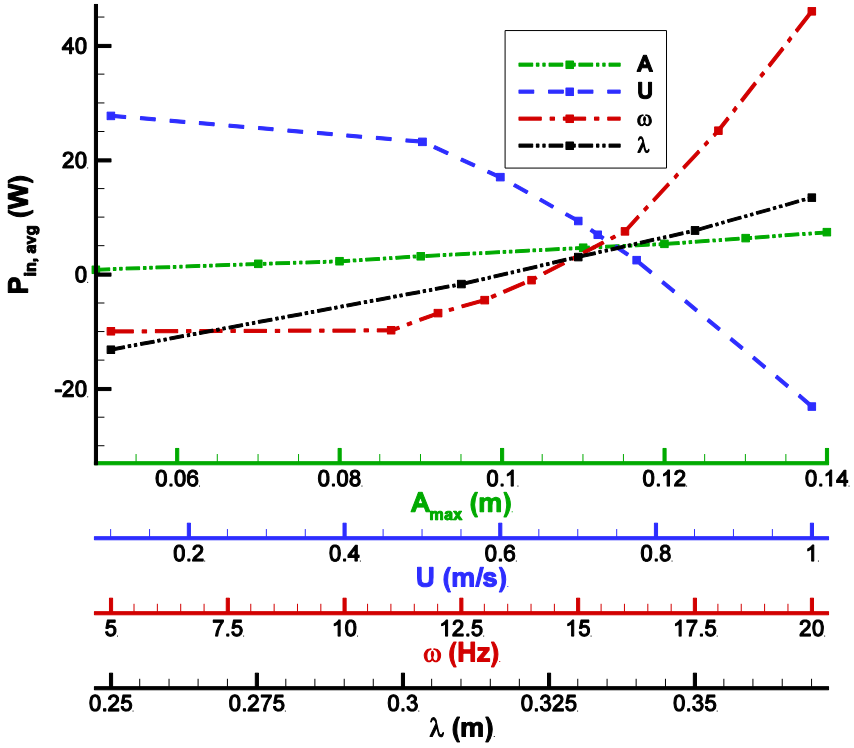


*Figure 2-9: Effect A, $U_\infty$, ω, and λ have on $P_{in}$.*

The parametric relationships for power output tend to be similar (though not identical) to those for power input, as seen in Figure 10. The general relationships (quadratic or linear) are the same for velocity, frequency, and wavelength, although they are shifted relative to the input power relationships. Additionally, the amplitude has negligible effect on the output power over the interval tested. This suggests that lower amplitude envelopes will tend to reduce power consumption with negligible effect on the output power of the system.

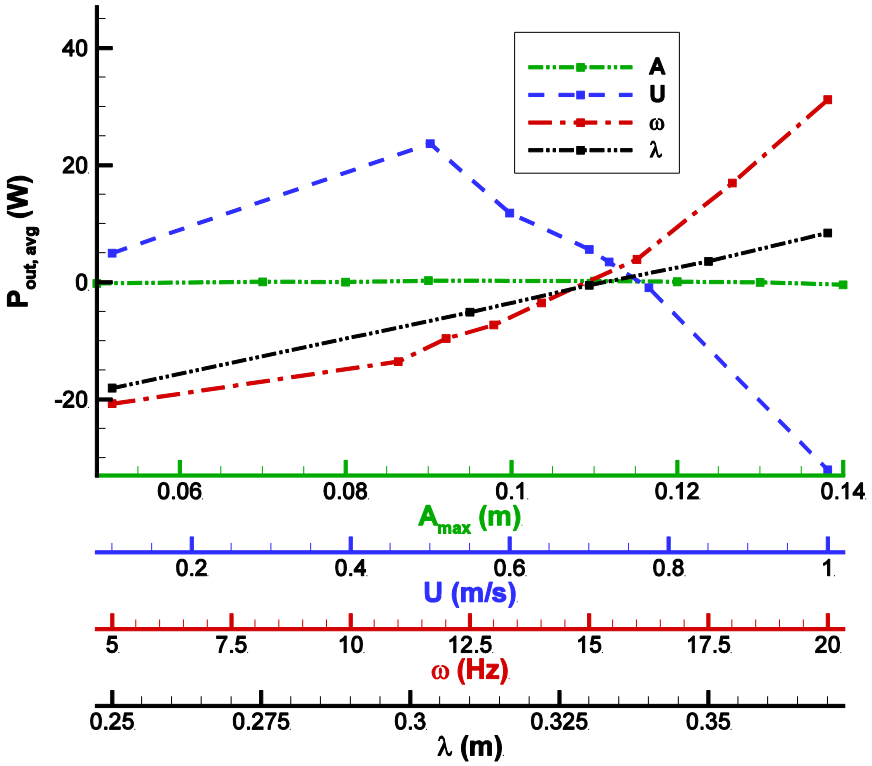


*Figure 2-10: Effect A, $U_\infty$, ω, and λ have on $P_{out}$.*

One common way to measure efficiency is the simple ratio of output power to input power. When this ratio is used for the previously given power characteristics, the resulting efficiency is as shown in Figure 11. On our given parametric intervals, the relationship between each parameter and the resulting efficiency is somewhat unclear due to the discontinuity corresponding to an input power of zero. A more clear depiction of the relationship between power input and output can be seen in Figure 12.

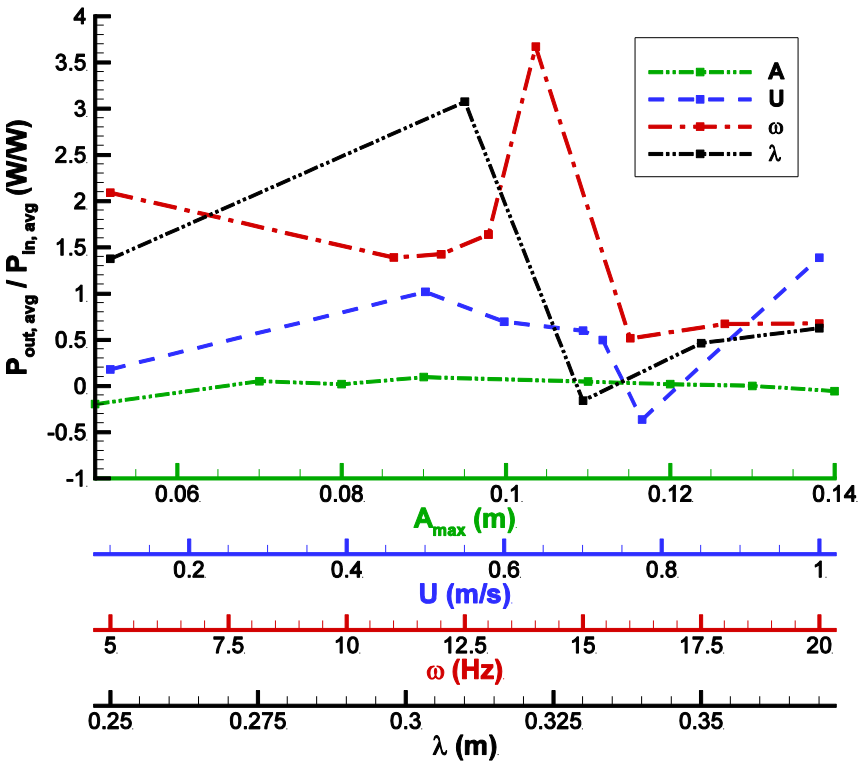


*Figure 2-11: Effect A, $U_\infty$, $\omega$, and $\lambda$ have on $P_{in}/P_{out}$.*

Note from Figure 12 that the amplitude cases all show a direct effect on input power with negligible change in output, as previously discussed. However, for the other parameters (velocity, frequency, and wavelength), the relationship between power in and power out is nearly linear, regardless of the kinematics themselves. Based on this relationship, a more representative way to define efficiency $\eta$ near the origin could be according to

$$\eta = \frac{\partial P_{out}}{\partial P_{in}} \tag{22}$$

Farther away from the origin, this relationship would be less useful, at which point the more typical ratio $P_{out}/P_{in}$ would be more relevant and less affected by the discontinuity at $P_{in} = 0$. Note also that this relationship does have a small negative concavity, meaning that the linear approximation around the origin will not hold for more extreme cases. Further study could be taken to determine the more representative relationship between the power characteristics for more extreme cases of input or output power.

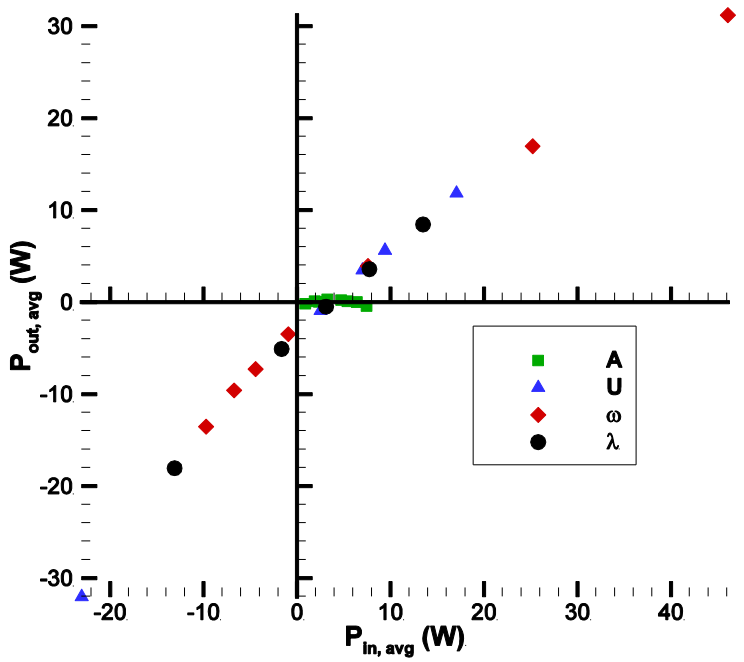


*Figure 2-12: A comparison of $P_{in}$ and $P_{out}$*

### 2.5. Conclusion

CFD was used to simulate a two-dimensional representation of an undulatory stingray fin. The fin was modeled as a sinusoidal wave with linearly increasing amplitude. Laplacian smoothing and diffusion remeshing were used to prevent mesh degradation around the deformable boundary.

Based on the CFD results for a parametric study of the kinematics, the frequency, wavelength, and swimming speed each showed significant effects on horizontal force production (in the direction of the flow), whereas wave amplitude did not. When compared to the literature, this trend for the two-dimensional case suggests that amplitude affects thrust production primarily due to out-of-plane fluid dynamics. As the magnitude of the horizontal forces increases, the body experiences significant average and RMS pitching moments. Furthermore, the RMS lift was found to be quite large compared to the drag and thrust forces. Although the large planform typical for stingrays is expected to act like a flat plate, resisting the effects of the RMS moment and lift on the body, these effects should be considered when designing a robotic system using undulatory locomotion. Similarly, the average pitching moment should also be considered for stability when designing a control system utilizing undulatory fins.

In addition to the forces and moments, the power input and output were also considered for the system. Because the amplitude showed minimal effect on the horizontal force production, it also had minimal effect on the power output of the system. However, increasing the amplitude also increased the power input required to drive the fin, suggesting that amplitude changes may not be the most efficient method for controlling swimming speed. Meanwhile, for constant amplitude, the power output was found to correspond exclusively to the power input, regardless of the particular kinematics used to achieve that power input. This trend means that power losses for the system are independent of the particular kinematic parameters prescribed, and rather depend on the overall power input instead. Additionally, the results indicated that negative power input was possible when the system was subject to deceleration. Such results suggest that undulatory propulsion may provide an opportunity for regenerative braking, allowing a robotic system to recover power from the fluid.

One last point of note is the method of determining efficiency for an undulatory propulsion system. For this study, power input was determined based on the vertical forces and speeds required to drive the system in the computed fluid flow (corresponding to a typical robotic system), while the power output was defined by the resulting horizontal forces at a given speed. The results suggested that there is a direct, nearly linear relationship between power input and output, but because the range of power input requirements can cross from positive to negative, and because the relationship is offset from the origin, a simple ratio of power output to input is not sufficient to define efficiency. One possible way to mitigate this issue is to use the derivative of power output with respect to power input when near the origin. This slope decreases with increasing power output, meaning that as with any system, there are trade-offs when designing for energetic efficiency versus for speed and performance.

The aim of this parametric study was to demonstrate the effect of each kinematic parameter in the wave equation on the average and variance of resulting forces and moments on the undulatory body. Ultimately, these reactions and the observed power characteristics can be used to design and optimize a robotic system using undulatory propulsion.

### 2.6. References

[1] Webb, P. W., 1984. “Form and Function in Fish Swimming”. *Scientific American*, ***251***(1), pp. 72–82.

[2] Rosenberger, L. J., 2001. “Pectoral fin locomotion in batoid fishes: undulation versus oscillation”. *Journal of Experimental Biology*, ***204***(2), pp. 379–394.

[3] Lighthill, J., and Blake, R., 1990. “Biofluiddynamics of balistiform and gymnotiform locomotion. Part 1. Biological background, and analysis by elongated-body theory”. *Journal of Fluid Mechanics*, ***212***, pp. 183–207.

[4] Eloy, C., 2012. “Optimal Strouhal number for swimming animals”. *Journal of Fluids and Structures*, ***30***(1), pp. 205–218.

[5] Rosenberger, L. J., and Westneat, M. W., 1999. “Functional morphology of undulatory pectoral fin locomotion in the stingray taeniura lymma (chondrichthyes: Dasyatidae)”. *Journal of Experimental Biology*, ***202***(24), pp. 3523–3539.

[6] Blevins, E. L., and Lauder, G. V., 2012. “Rajiform locomotion: three-dimensional kinematics of the pectoral fin surface during swimming in the freshwater stingray potamotrygon orbignyi”. *Journal of Experimental Biology*, ***215***(18), pp. 3231–3241.

[7] Curet, O. M., Patankar, N. A., Lauder, G. V., and MacIver, M. A., 2011. “Aquatic manoeuvering with counterpropagating waves: a novel locomotive strategy”. *Journal of the Royal Society Interface*, ***8***(60), pp. 1041–1050.

[8] Low, K., 2011. “Current and future trends of biologically inspired underwater vehicles”. In Defense Science Research Conference and Expo (DSR), 2011, IEEE, pp. 1–8.

[9] Chen, J., Hu, T., Lin, L., Xie, H., and Shen, L., 2010. “Learning control for biomimetic undulating fins: An experimental study”. *Journal of Bionic Engineering*, 7, pp. S191–S198.

[10] Jones, M., and Joordens, M., 2014. “Design of an angular radial robotic stingray”. In World Automation Congress (WAC), IEEE, pp. 234–239.

[11] Liu, F., Yang, C. J., and Lee, K. M., 2010. “Hydrodynamic modeling of an undulating fin for robotic fish design”. IEEE/ASME International Conference on Advanced Intelligent Mechatronics, AIM, pp. 55–60.

[12] Sfakiotakis, M., and Fasoulas, J., 2014. “Development and experimental validation of a model for the membrane restoring torques in undulatory fin mechanisms”. In 22nd Mediterranean Conference on Control and Automation (MED), pp. 1540–1546.

[13] Wei, Q. P., Wang, S., Dong, X., Shang, L., and Tan, M., 2013. “Design and kinetic analysis of a biomimetic underwater vehicle with two undulating long-fins”. *Acta Automatica Sinica*, ***39***(8), pp. 1330–1338.

[14] Zhu, J. Y., and Zhou, C. Y., 2014. “Aerodynamic performance of a two-dimensional flapping wing in asymmetric stroke”. *Proceedings of the Institution of Mechanical Engineers Part G-Journal of Aerospace Engineering*, ***228***(5), pp. 641–651.

[15] Blevins, E., and Lauder, G. V., 2013. “Swimming near the substrate: a simple robotic model of stingray locomotion”. *Bioinspiration & Biomimetics*, ***8***(1), p. 016005.

[16] Clark, R., and Smits, A., 2006. “Thrust production and wake structure of a batoid-inspired oscillating fin”. *Journal of Fluid Mechanics*, ***562***(1), pp. 415–429.

[17] Rahman, M. M., 2013. “Study on biomimetic squid-like underwater robots with two undulating side fins”. PhD thesis, Osaka University.

[18] Zhang, Y., Laibin, J., He, J. H., Yang, J., Zhang, S., and Low, K. H., 2006. “A numerical analysis of an undulatory mechanical fin driven by Shape Memory Alloy”. *2006 IEEE International Conference on Robotics and Biomimetics, ROBIO 2006*, ***4***, pp. 73–78.

[19] Zhijun, W., Weishan, C., and Shengjun, S., 2013. “Influence of pectoral fin amplitude on batoid locomotion”. *International Journal on Advances in Information Sciences and Service Sciences*, ***5***(7), pp. 129–137.

[20] Shirgaonkar, A. A., Curet, O. M., Patankar, N. A., and MacIver, M. A., 2008. “The hydrodynamics of ribbon-fin propulsion during impulsive motion”. *Journal of Experimental Biology*, ***211***(21), pp. 3490–3503.

[21] Sharp, N., Hagen-gates, V., Hemingway, E., Syme, M., Via, J., Feaster, J., Bayandor, J., Jung, S., Battaglia, F., and Kurdila, A., 2014. “Computational Analysis of Undulatory Batoid Motion for Underwater Robotic Propulsion”. In Proceedings of the ASME 2014 4th Joint US-European Fluids Engineering Division Summer Meeting, pp. 1–8.

[22] Gater, B., Kossobokova, L., Royston, W., Walsh, M., Croson, M., Arendt, D., Mull, J., Capella, N., Hosseinian, M., Feaster, J., Matta, A., Horton, B., Battaglia, F., Jung, S., and Bayandor, J., 2015. “Unsteady hydrodynamic robotic concept for high-density fluid environments”. In Proceedings of the ASME-JSME-KSME Joint Fluids Engineering Conference 2015, pp. 1–6.

[23] ANSYS Incorporated, 2014. *Fluent 15.0 User’s Guide*.

## 3. Paper #2: Power Regeneration of a Bioinspired Electromechanical Propulsive Fin

### 3.1. Abstract

*Bioinspired swimming methods have become highly attractive due to the potential for low environmental impact and high efficiency. However, although the efficiency has been quantified for select robotic and theoretical models, this paper explores more directly how requisite power consumption of an undulatory fin is affected by desired swimming speed. It further introduces and quantifies a method for recovering energy from the flow. First, CFD was used to simulate a cross-section of a fish fin with a wave number of 1.2 and a linearly increasing amplitude envelope. Flow speed and fin wave frequency were varied to determine interactive effects on force production and power requirements. The data from these simulations was fitted with polynomial functions over the range used for the study. To determine the potential for power regeneration from the flow, the fin was augmented with a mathematical model of a DC motor and shaft driving it. By incorporating the motor model into the fin analysis, the authors analyzed the amount of power input, or power regeneration, into the system from a constant velocity fluid flow, and developed a relationship between flow velocity and power regeneration. This relationship provides insight into both the level of power regeneration for the fin if held fixed in constant flow, and the minimum flow speed to regenerate energy at a desired rate. The determination of the relationships between efficiency and mode of operation will provide insight into the energetic efficiency of robotic designs using this method. Furthermore, the possibility of power recovery could pave the way for longer lasting underwater robots in extended missions. The determination of both efficiency and power regeneration capability will provide insight into the energetic feasibility of using, and improving on, the current capabilities of bioinspired underwater propulsion.*

### 3.2. Introduction

Recently, technological advances in computers, mechatronics, and control methods have facilitated the development and plausibility of using robotic vehicles for exploration. As the field of ocean engineering witnesses the development of new submersible vehicles that traverse and explore seas and oceans, the need for efficient propulsion and greater maneuverability for discovering the unknown undersea environment necessitates research into methods of transport

other than propellers and jets. To address the need, researchers have turned to biological mechanisms for inspiration.

Commonly, biological mechanisms such as fish propulsion are thought to be more efficient than engineered mechanisms due to optimization through natural selection. However, nature selects for more than just propulsive efficiency, and biological actuation methods (e.g. muscles) are configured quite differently than engineered ones (e.g. DC motors). As such, it is of interest to quantify the force and power characteristics of the bioinspired systems to determine their utility during application.

This particular study focuses on underwater fluid dynamics of a fin mechanism inspired by an undulatory stingray. Rays use their pectoral fins to pass an undulatory wave from anterior to posterior, thereby propelling themselves forward [1]. This wave can be modelled as a travelling sinusoid, and is similar in kind to a general fish model using motion parameters such as amplitude, frequency, and wave number to control motion and speed [2]. A variety of methods, ranging from analytical [2–4] to experimental to computational [5-7] can be used to make observations about fish swimming methods, wake development, force characteristics, and power requirements for this type of bioinspired propulsion.

Efficiency estimates for fish swimming have been approached in a variety of ways. For example, Moored et al [8] used both analytical and experimental methods to determine and verify that the peaks of propulsive efficiency occur when a fin flaps at the resonant frequency of the jet profile. An experimental study, Anderson et al [9] found experimentally that an oscillating foil in water with high angle of attack could produce a propulsive (Froude) efficiency as high as 87% in a case of net thrust. Rahman et al [5] determined a peak efficiency closer to 20% for their undulatory fin, again during a case of net thrust. As noted in Borazjani and Sotiropoulos [10], however, the Froude efficiency equation for propulsion is only meaningful when under equilibrium conditions, when the net average force acting on the body is 0. Their calculated efficiency, using a decomposition of forces to determine thrust at a total net force of 0, showed carangiform swimming efficiency at almost 50%. This sort of analysis in regards to power and efficiency is fairly typical, where only cases of net positive thrust (acceleration) or net 0 thrust (equilibrium) are considered. However, CFD results from [11] suggest that when experiencing net drag (deceleration of a free body), an undulatory fin may be able to recover power from the surrounding fluid, though this capability has not been explored in the literature.

Power recovery, or regeneration, is of interest primarily to lengthen the feasible timespan of robotic missions. By modelling the fin as being actuated via a single motor and crankshaft, the capacity for power regeneration can be explored more readily than typical multi-motor models. In the fields of electrical engineering and mechatronics, it is commonly accepted that by using an appropriate H-bridge configuration to control and provide power to the motor, it is possible for a back-driven motor to provide power back to a battery [12]. By combining the fluid model with an electronic motor model, we can quantify both the amount of power required to propel an undulatory fin through the water as well as the amount of power than can be regenerated by the same fin when fixed in the presence of constant flow.

### 3.3. Methodology

In this paper, CFD is used to gather data showing the effect of fin frequency and flow velocity interaction on drag and power production. Using empirical models to represent the data, the power input to the fin required to achieve a desired swimming speed was determined in the range 0 – 1 m/s. Additionally, we determined the maximum power obtainable from using regeneration in the same range of flow speeds. The following subsections discuss in more detail the methods and theory used in the analysis.

#### *3.3.1. Fin Model*

A wavy plate was used as a 2D transverse cross-section representation of a stingray fin. The motion of the plate was modeled as a travelling wave equation such that the vertical displacement $y$ at time $t$ of a point distance $x$ from the leading edge of the fin can be represented as

$$y(x,t) = A(x)\sin\left(2\pi\left(n\frac{x}{L} - ft\right)\right) \quad (1)$$

where $A(x)$ is the amplitude envelope, $L$ is the length of the fin, $n$ is the wave number (number of sinusoidal periods present on the fin at one time), and $f$ is the frequency. For this study, the amplitude envelope was chosen to be $A_{max}\left(\frac{x}{L}\right)$, such that the amplitude of the wave increases linearly from 0 at the leading edge to $A_{max}$ at the trailing edge. Figure 1 shows an annotated diagram of the travelling wave on the fin, where the flow speed $U$ encounters the leading edge on the left, and the wave number is given by $n = L/\lambda$, where $\lambda$ is the wavelength of the traveling wave.

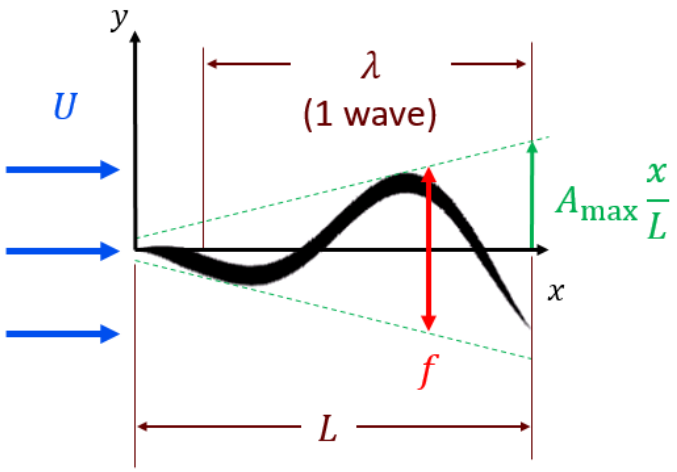


*Figure 3-1: Flow speed $U$ over the simulated fin of length $L$ with kinematic parameters wavelength $\lambda$, maximum amplitude $A_{max}$, and frequency $f$.*

In this study, the flow speed $U$ was varied in the range $0.1 - 1$ *m/s*, and the frequency was varied in the range $0.5 - 3$ *Hz*. The wave number was held constant at 1.2, within the undulatory regime for stingrays. The slope of the amplitude envelope was 0.25, based on the region of increasing amplitude of the undulatory stingray *Potamotrygon orbignyi* [13]. The length of the fin was set at 0.4 *m* to represent the size of a feasible robotic design. For total fin power characteristics discussed in the regeneration section, the width of the fin was taken as 0.2 *m* for an aspect ratio of 0.5, and the amplitude of the wave along the width at a particular point $x$ was assumed constant to simplify analysis and avoid 3D effects.

### *3.3.2. Computational Fluid Dynamics*

The fluid mechanics resulting from the dynamic motion of the 2D fin cross-section were solved using ANSYS Fluent (v. 16.0). For the unsteady, incompressible flow of the water over the fin, the continuity and momentum equations are

$$\nabla \cdot \vec{v} = 0 \tag{2}$$

$$\rho\left[\frac{\partial^2 \vec{v}}{\partial t^2} + \vec{v} \cdot (\nabla \vec{v})\right] = -\nabla p + \mu \nabla^2 \vec{v} \tag{3}$$

where $\rho$ is density, $p$ is pressure, $\mu$ is viscosity, and $\vec{v}$ is the velocity vector of the fluid. In Fluent, the flow was solved with the segregated pressure-based Navier-Stokes (PBNS) method with the semi-implicit method for pressure linked equations (SIMPLE) algorithm to resolve the pressure-velocity coupling. Gradients were discretized with the least squares cell based (LSCB) method,

momentum equations were discretized as second order implicit, and time was discretized as first-order implicit. The maximum time step for a particular simulation was chosen based on a version of the Courant-Fredrichs-Levy (CFL) number

$$CFL = \frac{V\Delta t}{\Delta x} \tag{4}$$

where $V$ is either the flow speed or the vertical velocity of the trailing edge of the fin (whichever was largest), $\Delta t$ is the time step, and $\Delta x$ is the smallest cell size. The Reynolds number ranged between approximately $4 \times 10^4$ and $4 \times 10^5$ for all cases. Because the Reynolds number remained below the critical Reynolds number ($5 \times 10^5$) for all cases, a laminar flow model was used.

The mesh domain was $11.2 \times 8\ m$, with $7L$ in front of the leading edge of the fin, $20L$ behind the trailing edge of the fin, and $10L$ above and below the fin. Water enters the computational domain along the left boundary (-$x$) with a specified uniform velocity $U$. The upper and lower boundaries of the domain are modelled as symmetric boundaries, and the right boundary is set at an ambient pressure of $p = 0$. Within the domain, an unstructured finite-volume mesh is used around the cross-section and updated each time step using a diffusive smoothing method to retain conformity to the dynamic fin cross-section. The diffusive smoothing is modelled as

$$\nabla \cdot \left(\gamma \nabla \vec{\psi}\right) = 0 \tag{5}$$

where the diffusion coefficient $\gamma$ determines the extent to which the boundary motion $\vec{\psi}$ propagates through the surrounding mesh region. $\gamma$ can be calculated according to the cell distance $d$ from the deforming boundary

$$\gamma = 1/d^a \tag{6}$$

where $a = 1.75$ was the diffusion parameter used in these simulations. The mesh used a minimum of 266,262 cells for all simulations. Figure 2 shows the mesh near the fin at the beginning of the simulation.

A grid convergence study was performed on the mesh to estimate the numerical accuracy of the solution by evaluating the relative difference of an increasingly fine mesh with respect to parameters of interest, such as average drag [14]. The mesh for this study showed 3rd order accuracy, with a 0.24% error in determining drag at 1.0 *m/s*, and a 6.65% error in determining drag at 0.1 *m/s*.

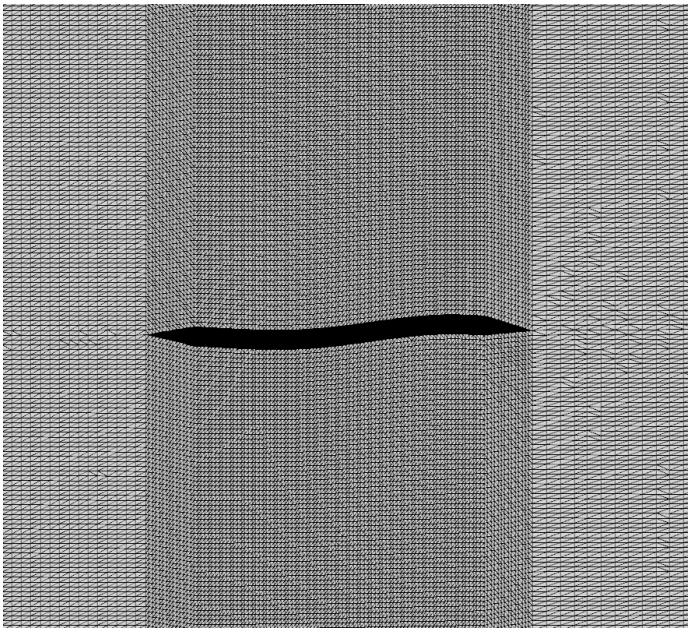

*Figure 3-2: Mesh around the fin used for the CFD simulation.*

### *3.3.3. Mechanical Power Estimation*

By assuming that the fin is driven by actuators that act transverse to the fin (denoted as the $y$-direction in accordance with the CFD model) the differential power input from the actuator(s) to the fin is

$$dP_{fin} = F_y v_y dA \tag{7}$$

and by integrating along the length, the total power input from the actuator(s) are

$$P_{fin} = \int_0^L (F_y v_y) w \, dx \tag{8}$$

Note that $P_{fin} > 0$ here indicates that the motor induces force from the fin into the fluid to act in the same direction as the velocity at a point, while $P_{fin} < 0$ indicates that the fluid induces force from the fluid to the fin in the same direction as the velocity at that point.

### *3.3.4. Data Fitting*

The drag and power data from varying frequency and velocity (while holding length, wave number, and amplitude constant) were extracted from the CFD results to quantify the relationship between kinematics parameters and resulting fin force or required power input. Based on the data, the drag was modelled quadratically with frequency and velocity, and power was modelled as

varying cubically with frequency and velocity. Coefficients for the models were determined using regression analysis on the data.

### *3.3.5. Motor – Regeneration*

Suppose that a fin with a specific prescribed wavelength and amplitude is driven by a single DC motor through a theoretical mechanism akin to a crankshaft. In this model, the rotational speed of the shaft of the motor is the same as the frequency $f$ of the fin, and the power and torque transmit between the fin and motor with 100% efficiency. Note that most DC motors are designed to produce relatively high velocity and low torque, so a gearbox would also be required to bring the velocity and torque into a range more appropriate for this application. In this analysis, the gearbox will also be assumed 100% efficient.

For the motor model, transient responses resulting from the inner circuitry (such as inductance and capacitance) are assumed to be negligible. Instead, the analysis will focus on the electromagnetic force component of the motor, which is the basis for the conversion of electrical energy to mechanical energy (and vice versa). By focusing on this element, a relationship between motor power and rotational frequency is developed, incorporating losses from motor efficiency and internal resistance.

This section will focus on regeneration, in which power flows from the fin into the motor, which will in turn provide power to the battery. Then the mechanical power from the fin into the motor $P_{mech}$ can be represented as

$$P_{mech} = \tau\omega \tag{9}$$

where $\tau$ is the torque on the motor and $\omega$ is the speed of the motor. The power provided to the motor from the fin can also be represented electrically by considering the circuitry, including internal resistance that causes power loss to heat:

$$P_{elec} = P_{regen} + P_{res} \tag{10}$$

$$\eta P_{mech} = P_{regen} + I^2R \tag{11}$$

where $P_{res}$ is the power dissipated over the resistor, $I$ is the current flowing through the motor due to the input torque, and $R$ is the internal resistance of the motor.

Due to the electromotive force from the motor, additional equations relating the mechanical to the electrical system can also be used:

$$I = \frac{\eta}{k_g k_t}\tau \tag{12}$$

where $V$ is the voltage across the motor due to its rotation, $\eta$ is the efficiency of the motor, $k_g$ is the gear ratio, $k_t$ is the torque constant, $k_e$ is the electromotive force (EMF) constant, and $k_e = k_t$. Using these relationships, $P_{regen}$ can be expressed in terms of the torque and frequency:

$$P_{regen} = \eta\tau\omega - \left(\frac{\eta}{k_g k_t}\tau\right)^2 R \tag{13}$$

Then, using the fitted model from the CFD data, we have a relationship between torque and frequency of the fin at a known flow speed $U$. This relationship from the CFD results in mechanical fin power due to the flow $P_{fin}(\omega, U) = \tau\omega$ that can be substituted into the previous equation such that

$$P_{regen} = \eta P_{fin}(\omega, U) - R\left(\frac{\eta}{k_g k_t}\right)^2 \left(\frac{P_{fin}(\omega,U)}{\omega}\right)^2 \tag{14}$$

which at a given speed $U$ will allow a maximum value for $P_{regen}$. The desired value of $P_{regen}$ will determine the resulting fin frequency and torque, as well as the voltage and current across the motor. This analysis will determine the maximum $P_{regen}$ at a given flow speed $U$. Alternatively, the equation could be solved to determine the minimum flow speed necessary to provide the desired $P_{regen}$.

### *3.3.6. Motor – Drive*

When analyzing a propulsive system, it is also practical to consider the necessary drive power to produce 0 net drag. Because 0 net drag occurs when the vehicle maintains a constant average swimming speed, the power characteristics at this point correspond to the typical requisite power consumption to maintain a desired swimming speed. In this case, $P_{mech}$ is the power acting on the fluid from the fin. Applying the motor efficiency in this direction,

$$P_{mech} = \eta P_{elec} \tag{15}$$

such that $P_{elec}$ is simply the power drawn from the battery.

For the purpose of comparison, the motor model used for this paper is based on a 30 *W* brushless Maxon motor with $k_t = 2.54$ *mN·m*, and maximum efficiency of 79%. For the purposes of this paper, the efficiency was set at $\eta = 0.75$. The gear ratio $k_g$ was chosen to be 106 in this example to increase stall torque to 8 *N·m* and decrease maximum frequency to 7 *Hz*.

## 3.4. Results

After processing CFD results from various combinations of velocity and frequency, useful data can be extracted from the time histories of the fluid flow over the fin, such as net horizontal force (drag or thrust, depending on the sign) and power input (the power required to drive the fin at that swimming speed and frequency).

### *3.4.1. Fluid Force and Power Curves*

The resulting drag curves are shown at different velocities with respect to frequency in Fig 3, and can be modeled with quadratic curves with respect to both frequency and velocity ($R^2 = 0.9986$). These curves show that net drag is produced when the frequency is too low for the swimming speed, and net thrust when the frequency is relatively high for the given swimming speed. For constant kinematics (frequency), the fin would tend to come to a final "steady swimming speed" where the drag is approximately zero. (Note that body drag in this analysis is neglected). Because the drag is approximately quadratic with respect to both velocity and frequency, the steady swimming speed is approximately proportional to the frequency, as shown in Fig 4.

Meanwhile, the power input as a function of frequency at different swimming speeds is shown in Fig 5. The power input here is modeled as approximately cubic with respect to velocity and frequency ($R^2 = 0.9982$). At high frequencies (which generally produce acceleration/thrust as shown in the drag results), the power input required is positive, meaning simply that a power supply must provide power to the motor to allow the fin to continue to move at the desired frequency. At low frequencies (generally corresponding to deceleration/drag), the power input is negative, suggesting that power can be recovered from the fluid.

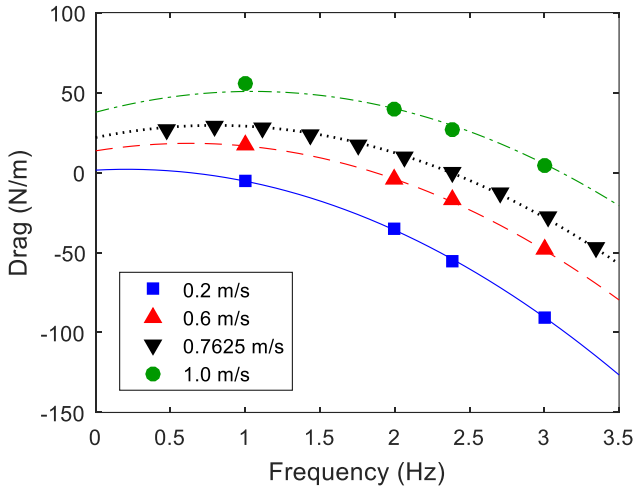


*Figure 3-3: Model quadratic fits for net average horizontal force (drag > 0) as a function of frequency at different flow speeds.*

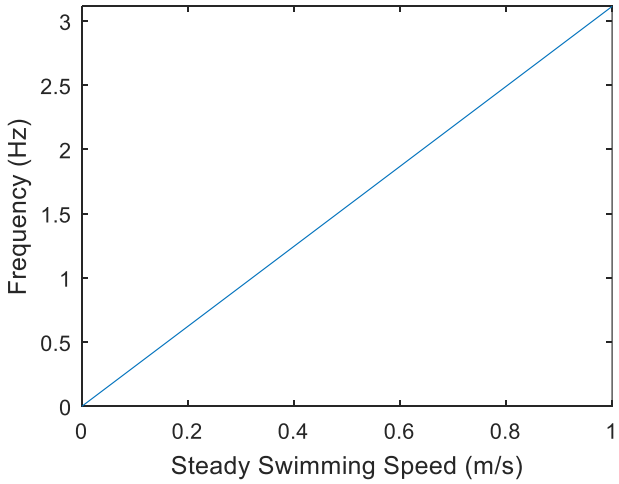


*Figure 3-4: Necessary fin frequency to maintain a desired steady average swimming speed.*

Using the relationship between frequency and steady swimming speed, the power input required to swim at an approximately constant speed can also be determined. Figure 6 shows the relationship between steady swimming speed and the ideal average input power (per width of fin) required to maintain that speed.

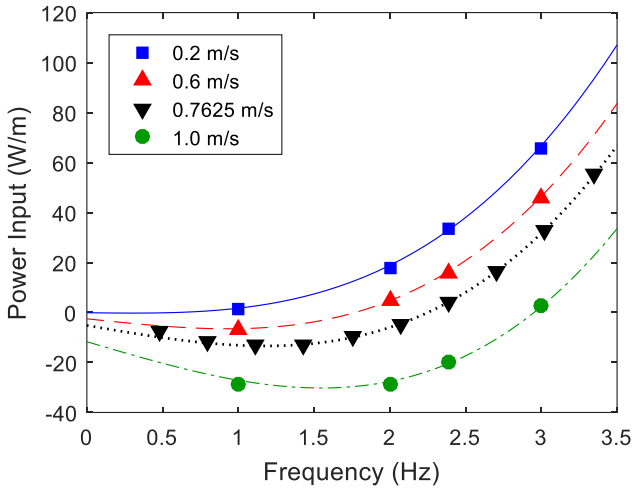


*Figure 3-5: Model cubic fits for net average power input as a function of frequency at different flow speeds.*

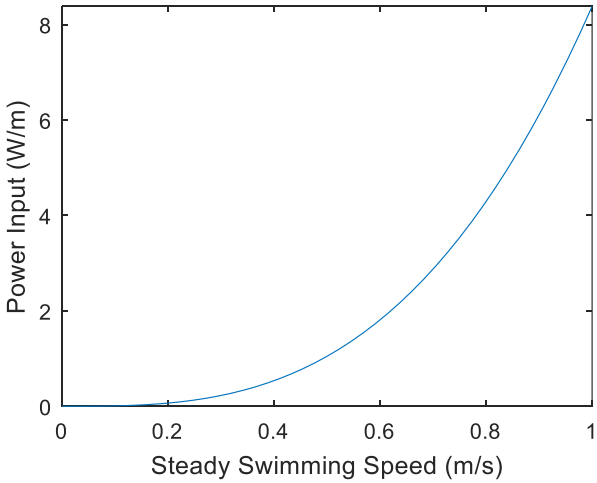


*Figure 3-6: Necessary power input per width of fin to maintain a desired steady average swimming speed.*

### *3.4.2. Regeneration*

From the motor model discussed previously, the power drawn by the motor from the fluid will be proportional to the square of frequency (for non-unity efficiency). Assuming that the fin is a particular width, such as 0.2 *m* wide, the power from the fluid can be calculated and compared to the power draw of the motor at different frequencies. Figure 7 shows the comparison of required

input power for constant velocity, as well as maximum regeneration in a constant velocity flow, where the solid curves correspond to the actual motor (75% efficient with internal resistance $R = 0.4\ \Omega$) and an ideal motor (100% efficient with 0 resistance).

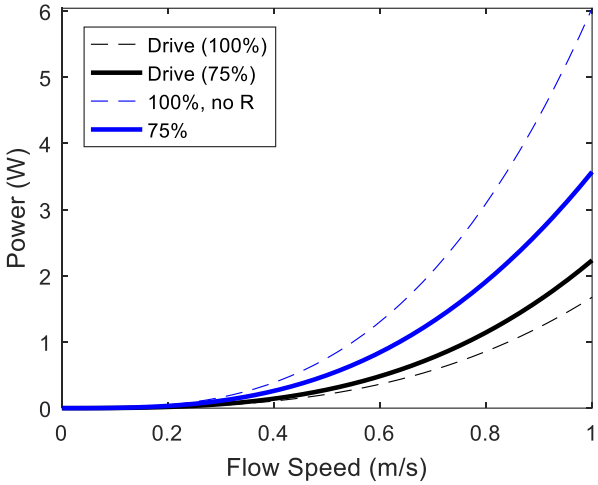


*Figure 3-7: Power needed to drive a 0.2 m fin at a steady swimming speed (blue), and power regeneration from a fin held fixed in a given flow speed (black).*

Interestingly, the maximum potential regenerative power in a constant flow speed is higher than the power required to travel at constant velocity at the same speed. Assuming the presence of a current, the power for the driving the motor to exactly counteract that flow speed will result in no net movement (relative to an inertial frame of reference). Meanwhile, the regeneration assumes that the fin is somehow fixed relative to the inertial frame, and the force of that fixed mount counteracting the force of the flow allows the fin to experience a higher net force (and thus regenerative power) than if the fin had to counteract the fluid force on its own. Additionally, when considering a real robot with significant body drag, this comparison would likely change significantly, since the robot would be operating in a higher thrust region that necessitates significantly more power to maintain constant velocity (note that the inclusion of a body would not significantly change the regenerative power). Additionally, as one would expect, inclusion of dissipative terms (such as efficiency and resistance) increase the power required for swimming at constant speed, and decrease the available power for regeneration.

To better understand the implications of the results discussed in the previous sections, a behavior of a 0.2 $m$ wide fin in a wide river that flows downstream at approximately constant velocity with uniform flow is considered (neglecting body drag once again).

Suppose the river flows at 0.25 *m/s*, and the fin travels at a groundspeed of 0.5 *m/s* in the desired direction during travel. Let us consider the relative regenerative capabilities when it wants to swim upstream, downstream, and across the river (neglecting the perpendicular current during swimming). In other words, consider the power requirements for traveling in a relative flow speed of 0.75 *m/s* upstream, 0.25 *m/s* downstream, and 0.5 *m/s* across.

Based on previous results, the fin requires 0.94 $W$ to travel upstream, 0.03 $W$ to travel downstream, and 0.28 $W$ to travel across the river. However, in all cases, the fin has approximately 0.07 $W$ available to regenerate from the flow. Assuming that the fin travels with periods of active travel to recharging time, the ratio of swimming to recharging time is 7% for the upstream case, 188% for the downstream case (i.e. can swim for about twice as long as the charging time), and 23% for the crossing case.

Practically, the results indicate that although the theoretical regeneration is higher for the fin (with negligible body drag) for a particular flow speed than the power required to swim at the same swimming speed, the comparison is somewhat more complicated, because travel speed needs to be taken into account as well. If the fin regenerates in a flow speed $U$, then traveling against the same current will require a higher relative flow speed (swimming upstream), and thus, a higher required power for travel due to the presence of a current.

### 3.5. Conclusion

Based on data obtained from the 2D CFD solutions, the net average horizontal force (drag or thrust) can be modelled as quadratic with respect to both velocity and frequency. Similarly, the average power input can be modelled as cubic with respect to velocity and frequency. Based on the force results, the fin frequency required to achieve a desired swimming speed is approximately proportional to that desired speed. This results in a cubic function of velocity describing the power input required by the fin to achieve the desired swimming speed.

Based on the regeneration results, it is indeed possible for a fixed undulatory fin to recover power from the surrounding fluid flow proportional to the cube of the flow speed. Although motor inefficiency and internal resistance reduce the maximum possible power regeneration, the overall power regeneration is still significant for a realistic motor, especially for high flow speeds.

In practice, the drive power for a desired swimming speed will be higher due to the presence of non-negligible body drag. However, the body drag should not strongly affect power

regeneration, given a sturdy mounting point to fix the body to an inertial frame (such as a rock or a wall). Instead, power regeneration methods would need to account for a motor-crankshaft mechanism efficiency, and for the effect of including a real (rather than perfect theoretical) charger circuit to convert the power of the motor to a voltage and current level appropriate for the battery. Further research could also include deeper analysis into methodologies for quickest or most efficient travel against an upstream flow.

The analysis presented in this paper offers insight into the feasibility of using power regeneration methods in a bio-inspired, undulatory fin mechanism designed for underwater travel. Such a method could provide a significant extension to mission lifetime and reduction of on-board power storage for a robot using undulatory fins for propulsion.

### 3.6. References


[1] L. J. Rosenberger, "Pectoral fin locomotion in batoid fishes: undulation versus oscillation.," *J. Exp. Biol*., vol. 204, no. Pt 2, pp. 379–394, 2001.

[2] J. Lighthill and R. Blake, "Biofluiddynamics of balistiform and gymnotiform locomotion. Part 1. Biological background, and analysis by elongated-body theory," *J. Fluid Mech*., vol. 212, pp. 183–207, 1990.

[3] M. J. Lighthill, "Aquatic animal propulsion of high hydromechanical efficiency," *J. Fluid Mech.*, vol. 44, no. 2, p. 265, 1970.

[4] S. Alben, "On the swimming of a flexible body in a vortex street," *J. Fluid Mech.,* vol. 635, p. 27, 2009.

[5] M. M. Rahman, Y. Toda, and H. Miki, "Computational Study on a Squid-Like Underwater Robot with Two Undulating Side Fins," *J. Bionic Eng.,* vol. 8, no. 1, pp. 25–32, 2011.

[6] A. A. Shirgaonkar, O. M. Curet, N. A. Patankar, and M. A. MacIver, "The hydrodynamics of ribbon-fin propulsion during impulsive motion.," *J. Exp. Biol.,* vol. 211, no. 21, pp. 3490–3503, 2008.

[7] F. Liu, K. M. Lee, and C. J. Yang, "Hydrodynamics of an undulating fin for a wave-like locomotion system design," *IEEE/ASME Trans. Mechatronics*, vol. 17, no. 3, pp. 554–562, 2012.

[8] K. W. Moored, P. A. Dewey, A. J. Smits, and H. Haj-Hariri, "Hydrodynamic wake resonance as an underlying principle of efficient unsteady propulsion," *J. Fluid Mech.,* vol. 708, no. February 2015, pp. 329–348, 2012.

[9] J. M. Anderson, K. Streitlien, D. S. Barrett, and M. S. Triantafyllou, "Oscillating foils of high propulsive efficiency," *J. Fluid Mech*, vol. 360, pp. 41–72, 1998.

[10] I. Borazjani and F. Sotiropoulos, “Numerical investigation of the hydrodynamics of anguilliform swimming in the transitional and inertial flow regimes.,” *J. Exp. Biol.,* vol. 212, no. Pt 4, pp. 576–592, 2009.

[11] B. Gater, J. Feaster, F. Battaglia, and J. Bayandor, “Dynamics and propulsive efficiency of bio-inspired undulatory marine locomotion,” in ASME 2016 Fluids Engineering Division Summer Meeting, 2016.

[12] T. A. Haskew and E. M. Hill, “Regeneration mechanisms in a DC motor with an H-bridge inverter,” IEEE Int. Electr. Mach. Drives Conf. IEMDC 1999 - Proc., pp. 531–533, 1999.

[13] E. Blevins and G. V. Lauder, “Rajiform locomotion: three-dimensional kinematics of the pectoral fin surface during swimming in the freshwater stingray Potamotrygon orbignyi,” *J. Exp. Biol.,* vol. 215, no. 18, pp. 3231–3241, 2012.

[14] I. B. Celik, U. Ghia, P. J. Roache, and C. J. Freitas, “Procedure for Estimation and Reporting of Uncertainty Due to Discretization in CFD Applications,” *J. Fluids Eng,* vol. 130, no. 7, 2008.

## 4. Conclusion and Future Work

The results obtained from these studies are new and significantly add to the body of literature related to the understanding of bio-inspired swimming. The utility of a bioinspired system depends on an informed understanding of the underlying mechanics to make them efficient and competitive with current technologies. This work uses computational fluid dynamics to investigate these underlying mechanisms and apply them to understanding the energetics of the propulsor as well as harnessing them to harvest power from the environment for the most effective implementation.

The first noteworthy result of the parametric study was the effect of amplitude changes on thrust production, or rather, the lack thereof. Although the RMS forces and moment increased, as well as the power required to enable the increase in amplitude, the average thrust showed no significant change. Because previous literature predicts an increase in thrust with amplitude, we can conclude that the primary role of amplitude changes in speed control is through the formation of a leading edge vortex through oscillation at the anterior section of the fin. When considering only the trailing edge effects for an undulatory fin in the inertial regime, the difference between swimming speed and wavespeed is the driving factor in determining whether or not the fin experiences a net thrust or a net drag. Amplitude changes serve to augment thrust production by amplifying effects in the wake, but near the steady swimming condition, it only amplifies a balanced system, resulting in no change in the average horizontal forces. Because undulatory fish use a larger amplitude at the trailing edge than the leading edge, this observation could explain why many species of fish tend to use higher amplitude motions during acceleration than during steady swimming, regardless of speed. For robotics applications, this result suggests that a vehicle should use frequency or wavelength, not amplitude, to control the swimming speed, but amplitude changes could be used to increase the magnitude of acceleration or reduce to energy losses.

Another key result of the parametric study was the relationship between power input and output for the fin. The averaged energetic results for the velocity, frequency, and wavelength variation all lay along approximately the same curve. It is possible that the intercept, and even the slope, of this curve may depend on the amplitude of the fin wave. Given a particular amplitude envelope, however, the results suggest that the greatest determining factor in power output is the power input itself, regardless of the particulars of the swimming speed and waveform interactions. For robotic applications, the implication is that for a given geometry and amplitude envelope, a single power curve could be measured and incorporated into a closed loop controller to control average

swimming speed in a highly predictable way. Of course, these results may behave differently outside of this regime, as in the peaks of Froude efficiency often noted in other works. However, control systems may be far simpler to implement in this regime, and may be more viable when considered in light of different metrics of locomotor cost (such as cost of transport) where large accelerations are less necessary.

Upon further examination of frequency-velocity interactions, low order nonlinear models were shown to explain more than 99.8% of the data. For these models, drag varied quadratically with both frequency and velocity, while power input varied cubically. By analyzing the drag model for zero average drag, the steady swimming speed was shown to be proportional to frequency, suggesting a linear relationship between wavespeed and swimming speed with a slope dependent on the geometry of the waveform alone. Interaction between this linear model and the power input was used to develop a quadratic predictive model of power input required to maintain a steady swimming speed with the fin. This predictive model could be useful for optimizing speed to minimize the cost of transport, or determining how much stored energy is required for a particular excursion.

The last major result of this work was a model for the regenerative capability of a single-motor fin fixed in oncoming flow. The power input model discussed previously showed local minima for each velocity, representing the maximum possible power available for regeneration at the given flow speed. The model can also take into account motor efficiency and resistance, and predict the regenerative power and fin frequency for a given flow speed. For a realistic motor, the fin was shown to be capable of regenerating more power when fixed in a given flow then it would consume to move at the same flow speed. Although for a full robot the inefficiencies in the system would reduce the regenerative capability, this result does suggest that for a long-term mission, regeneration is a viable method for extending mission life indefinitely.

Continuations to this work could follow several different avenues. The first is a parametric study about additional steady swimming points to investigate how the effects of wavelength in particular vary with steady swimming speed. Nonlinear models for force and power could then be developed to describe the interaction of the kinematic variables with the force production and energetics. Another direction, also computational in nature, involves the extension of this work to a three-dimensional simulation environment. The third dimension would provide an opportunity

to investigate a more realistic fin to determine how out of plane effects differ from the two-dimensional findings, and relate the new findings more directly to a robotic system.

Given the intention of application of this work to robotics, however, the most natural course of action is to build an undulatory robot for experimentation. Tests of a single-fin system could be used to validate results of the computational study, or to more quickly investigate the parametric space with regard to forces and energetics. Using a motor-shaft system for actuation of the fin, coupled with charging circuitry, the effectiveness of regeneration in the presence of further inefficiencies could also be tested. Additionally, the parameter effects could also be incorporated into the development of a control model. Using knowledge about the energetics behind it, the controller could also be designed for optimal efficiency or speed with numerical techniques. The presence of effective low-order models discussed in this work suggest that numerical computations could be quite effective without unreasonable levels of computational cost. I intend to pursue the development of optimal control for an undulatory robot as the focus of my doctoral dissertation. As the field progresses in its understanding of swimming, better design principles for robots using undulatory fins will be developed for optimization of efficiency, speed, and maneuverability. With advances in understanding regarding the efficiency and energetic capabilities of bioinspired technology, the future of robotics becomes ever more viable for application to long-term, exploratory marine missions.

**Appendix A: Grid Convergence Study**

This appendix is for discussing the grid convergence study in more detail. This study was referenced in the body of the report, and is important for establishing the numerical accuracy of the CFD solution.

In CFD and other computational techniques for representing mechanical systems, it is important to ensure that the computational model represents the real world well. Part of this involves ensuring that the discretization process uses adequately small elements when computing a solution. To ensure this, we can perform a grid convergence study to quantify the effect of the mesh on the results. Celik et al [1] outlines a methodology for quantifying and establishing a convergence metric for the uncertainty due to the discretization of the mesh.

Briefly, the methodology for quantifying uncertainty involves examining the results for three or more mesh refinements and determining the level of convergence. For this study, three different mesh refinements were used (coarse, medium, and fine) with a ratio of element size of almost 3 for the fine to medium mesh, and a ratio of about 1.5 between the medium and coarse mesh. The same simulation was run for each of these meshes, and a metric in the solution chosen for comparison of the meshes. Using the relative mesh size and the different solutions (based on the chosen metric), the apparent order of the method and the approximate error in the solution can be calculated. After that, the order and error were used to calculate the grid convergence index (GCI) to quantify uncertainty in the metric due to the mesh at the fine and mid-size refinement level. The choice can then be made as to which mesh refinement to use to achieve a satisfactory balance of computational cost and uncertainty.

Because this study uses a range of parameters, I chose to study the grid convergence at the lowest and the highest flow speeds (0.1 m/s and 1.0 m/s), corresponding to the highest and lowest Reynolds numbers. The time step size was chosen to ensure that the CFL number remained less than one, and the reference size for remeshing was modified to match the minimum cell size for each mesh. Otherwise, parameters were unchanged for the different cases; remeshing and smoothing parameters were chosen as described in Section 2.

For calculating the grid convergence index, the average horizontal force per meter depth (i.e. the drag in the 2D simulation) was used as the metric of interest. Table A-1 shows the convergence results for each set of cases. Here, $N$ refers to the number of elements in the mesh, $r$ is a measure

of the ratio of cell sizes between the meshes, $\phi = D_{avg}$ is the measured average horizontal force per meter depth (drag) from each case, $p$ is the approximate order of the solution method, $\phi_{ext}$ is the estimated parameter value for an infinitely fine mesh, $e_a$ is the approximate error between the mid and fine mesh, and $GCI_{fine}$ and $GCI_{mid}$ refer to the grid convergence index (GCI) of the fine and mid-size meshes, respectively.

*Table A-1: Results of the GCI study at two flow speeds, using $D_{avg}$ as the metric.*

| | 0.1 m/s | 1.0 m/s |
|---|---|---|
| $N_1, N_2, N_3$ | 1199021, 161300, 65305 | 1199021, 161300, 65305 |
| $r_{21}$ | 2.7264 | 2.7264 |
| $r_{32}$ | 1.5716 | 1.5716 |
| $\phi_1$ | -59.6117 N/m | 28.0290 N/m |
| $\phi_2$ | -62.8640 N/m | 28.0830 N/m |
| $\phi_3$ | -76.4710 N/m | 35.6380 N/m |
| $p$ | 3.59 | 10.94 |
| $\phi_{ext}^{21}$ | -59.5205 N/m | 28.0290 N/m |
| $e_a^{21}$ | 5.46% | 0.19% |
| $GCI_{fine}^{21}$ | 0.19% | 4.11e-6 % |
| $GCI_{mid}^{32}$ | 6.65% | 0.24% |

Based on the results in Table A-1, the fine mesh shows excellent accuracy in terms of the discretization, and the mid-size mesh shows fairly good results as well. To examine the results in a different way, consider a comparison of the time histories of each set of results. The drag (D) and lift (L) results for the low speed (0.1 m/s) case are shown in Figure A-1. Qualitatively, the fine and mid-size meshes produced very similar results for both lift and drag, with the most significant difference appearing to be the phase. The coarse mesh, however, showed significantly different averages, RMS values, and even frequency for the drag case.

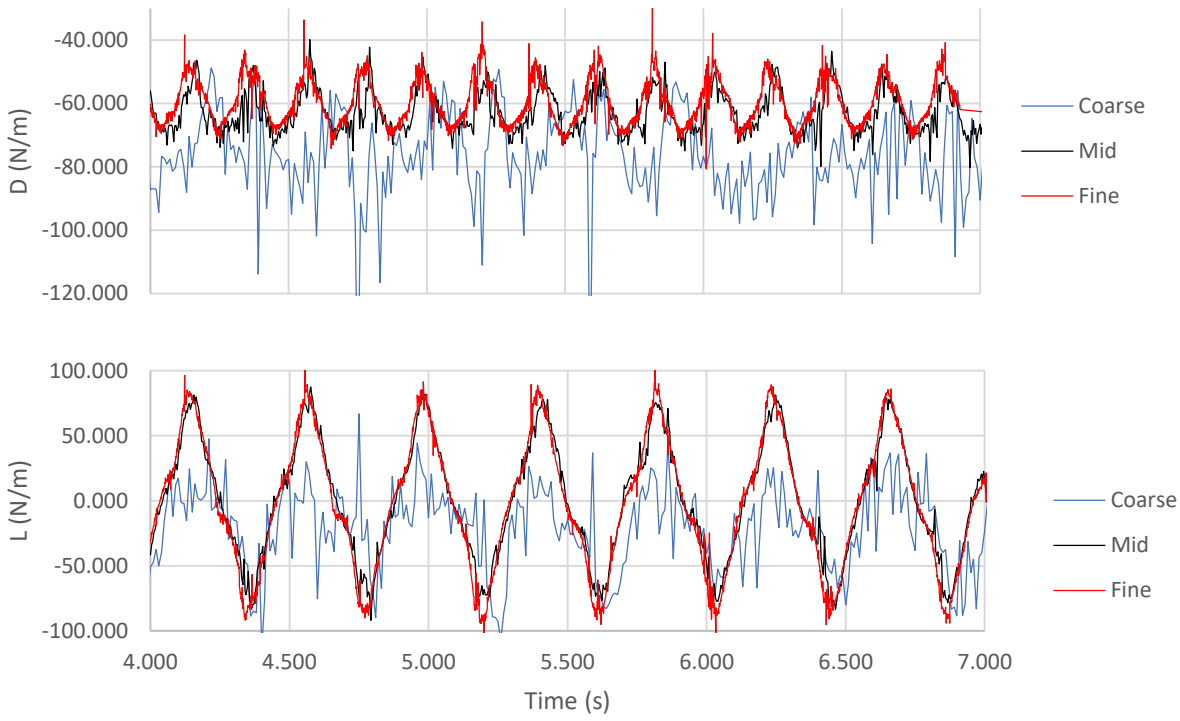


*Figure A-1: Lift and drag acting on the fin as a function of time for the three different mesh refinement levels with a 0.1 m/s flow speed.*

Next, the abridged convergence estimates for the low speed RMS lift and drag as well as the average lift are shown in Table A-2. The RMS drag shows fairly low error based on the GCI for both the fine and mid-size meshes. However, notice that the RMS drag for the coarse mesh ($\phi_3$) is about twice as high as for the fine and mid-size meshes ($\phi_1, \phi_2$). This is likely related to the frequency difference for the coarse mesh, which showed a single force period per flap cycle rather than two, and thus showed a greater effect for that single high amplitude period rather than for the two smaller amplitude periods of the finer meshes. Meanwhile, the average lift was fairly close to the expected of zero for the fine and mid-size meshes, but was very different for the coarse mesh, resulting in a low $GCI_{fine}$ but very high $GCI_{mid}$. From these results, it can be concluded that while the mid-size mesh produces adequately accurate results for $L_{avg}$, this measurement may be more susceptible to error than was the drag. Lastly, the RMS lift showed relatively more consistent results, with an excellent $GCI_{fine}$ of less than 1%, and a decent $GCI_{mid}$ of about 13%. From this, it seems reasonable to conclude that the mid-size mesh performs acceptably well in computing the results, although the lift results may be more susceptible to error.

*Table A-2: Results of the GCI study at a flow speed of 0.1 m/s for four force parameters as metrics.*

| | $D_{avg}$ (N/m) | $D_{rms}$ (N/m) | $L_{avg}$ (N/m) | $L_{rms}$ (N/m) |
|---|---|---|---|---|
| $\phi_1$ | -59.6117 | 7.039 | -1.024 | 49.228 |
| $\phi_2$ | -62.8640 | 6.775 | 1.118 | 44.864 |
| $\phi_3$ | -76.4710 | 13.813 | -18.971 | 32.028 |
| $GCI_{fine}^{21}$ | 0.19% | 0.00350 % | 2.31% | 0.61% |
| $GCI_{mid}^{32}$ | 6.65% | 5.26% | 301.05% | 12.83% |

Figure A-2 shows the lift and drag histories for the high speed (1.0 m/s) case. The fine and mid-size meshes again appear to agree fairly well, but the coarse mesh shows drastically different results. In fact, an even coarser mesh showed far better agreement with the fine and mid-meshes than this coarse mesh did, although the reasons for this are unclear. The drag shows a similar average, but a very different RMS value and, again, a frequency that is half the value expected. The lift, on the other hand, showed a very different average, but a comparable RMS and frequency value. Meanwhile, the fine and mid-size meshes agree very well for the lift results, but the histories themselves show significant computational noise relative to the amplitude of the resultant sinusoid. From this, we can fairly safely conclude that the mid-size mesh shows sufficiently accurate results, with the understanding that computational noise (which results from the residuals of error in the solution, which ranged from 1e-7 to 1e-5) can result in a relatively high signal to noise ratio for the RMS drag.

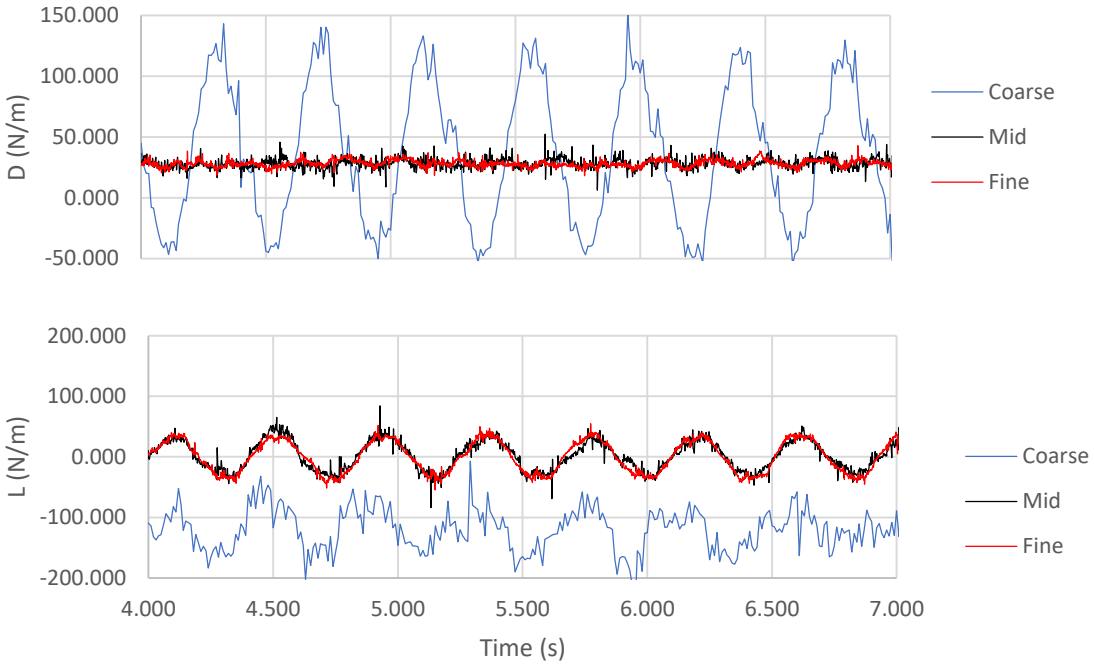


*Figure A-2: Lift and drag acting on the fin as a function of time for the three different mesh refinement levels with a 1.0 m/s flow speed.*

Before quantifying the computational noise, consider the GCI results for this 1 m/s case, as shown in Table A-3. As one would expect from considering the results qualitatively, the fine mesh shows an excellent GCI (less than 0.5%) due to its agreement with the mid-size mesh results, but the values for $GCI_{mid}$ are quite large due to the poor results from the coarse mesh. Based on a combination of the qualitative and quantitative results, it can be concluded that the mid-size mesh generally shows excellent results in terms of convergence to a "true" value, but for extreme cases may be susceptible to error during force quantification. The time history results for both the low and high speed cases seem to indicate that this large error is correlated with incorrect frequency results for the drag force (which should be twice the flapping frequency $f$), suggesting that the drag force frequency results could be used to indicate whether the force results on the whole are trustworthy. Even when the frequency indicator shows an issue, however, the average drag and RMS lift forces appear to be generally comparable to the actual values (with less than 20% error for $GCI_{mid}$). Because these two force values (average drag and RMS lift) are the primary forces of interest acting on the fin, it can be concluded that (1) the drag force frequency is a good indicator

of "poor" results, but (2) these "poor" results are still reasonably accurate for the two most important force parameters $D_{avg}$ and $L_{rms}$.

*Table A-3: Results of the GCI study at a flow speed of 0.1 m/s for four force parameters as metrics.*

| | $D_{avg}$ (N/m) | $D_{rms}$ (N/m) | $L_{avg}$ (N/m) | $L_{rms}$ (N/m) |
|---|---|---|---|---|
| $\phi_1$ | 28.0290 | 2.757 | 0.049 | 25.770 |
| $\phi_2$ | 28.0830 | 4.142 | 0.770 | 23.838 |
| $\phi_3$ | 35.6380 | 57.903 | -120.872 | 34.591 |
| $GCI_{fine}^{21}$ | 4.11e-6 % | 0.02% | 0.02% | 0.31% |
| $GCI_{mid}^{32}$ | 0.24% | 41.81% | 118.45% | 15.07% |

We can estimate the approximate uncertainty for each parameter in the mid-size mesh as:

$$u_\phi = \pm GCI_{mid} \times \phi_2 \quad \text{(A-1)}$$

The results of such estimation are shown in Table A-4, with the maximum uncertainty estimate shown as well. Based on these uncertainty estimates, all force parameter estimates appear to have an uncertainty less than 6 N/m.

*Table A-4: Uncertainty in each force metric for the mid-size mesh based on the results for each flow speed and Eq. A-1.*

| | $D_{avg}$ (N/m) | $D_{rms}$ (N/m) | $L_{avg}$ (N/m) | $L_{rms}$ (N/m) |
|---|---|---|---|---|
| 0.1 m/s: $u_\phi$ | 4.18 | 0.3564 | 3.3657 | 5.7561 |
| 1.0 m/s: $u_\phi$ | 0.0674 | 1.7318 | 0.9121 | 3.5924 |
| **Maximum $u_\phi$** | **4.18** | **1.7318** | **3.3657** | **5.7561** |

[1] I. B. Celik, U. Ghia, P. J. Roache, and C. J. Freitas, "Procedure for Estimation and Reporting of Uncertainty Due to Discretization in CFD Applications," *J. Fluids Eng*, vol. 130, no. 7, 2008.

**Appendix B: Validation**

Although not discussed previously in the thesis, validation is also a key part of numerical simulation. To validate the simulation, the CFD methods used must be shown to be capable of accurately solving similar flow physics. As discussed in Section 1, thin undulatory fins are known to produce a vortex street in the resulting wake. As such, the phenomenon we want to validate is this vortex street. One classic 2D case demonstrating a vortex street is a circular cylinder in cross-flow, so this is the one that was chosen for validation.

The validation case should match the system of interest in as many important details as is feasible. As such, the solver used was the same (e.g. unsteady incompressible Navier-Stokes, SIMPLE, PRESTO, QUICK!, etc.), and the mesh was a comparable level of refinement to the mesh used for the fin simulations. The cylinder had a 0.4 m diameter, and water was used for the simulation. To obtain the vortex street desirable for validation, the velocity was chosen to be 0.25 mm/s for a Reynolds of approximately 99.5.

Using these parameters, the simulation showed an average $c_D$ of 1.54, and average $c_L$ of -0.0018. The amplitude for each of these are 0.01 for $c_D$, and 0.35 for $c_L$. The results for the main cylinder used in Mittal & Raghuvanshi showed that for $Re = 100$, the averages are 1.40 for $c_D$ and 0 for $c_L$, while the amplitudes are about 0.01 and 0.35 respectively. Based on these results, the average drag $c_D$ shows an error of about 6.67%, while the average of $c_L$ (relative to its amplitude) amplitude of both drag coefficients appear to match quite closely.

Lastly, a common parameter to examine during vortex shedding is the Strouhal number $St$ of the resulting wake. The simulations showed a frequency of about 0.112 mHz, resulting in a $St$ of 0.179. The accepted value is approximately 0.168 [1]. As such, the error in $St$ is approximately 6.5%.

Based on this validation simulation, the methods and mesh used resulted in error less than 7% for both average drag coefficient and for the Strouhal number, while the average lift coefficients and amplitude of the drag and lift coefficient matched very well with the expected values. Although not perfect, this is an acceptable level of accuracy and suggests that the fin simulations used for the body of this work align well with reality.

[1] S. Mittal and A. Raghuvanshi, “Control of vortex shedding behind circular cylinder for flows at low Reynolds numbers,” *Int. J. Numer. Methods Fluids*, vol. 35, no. 4, pp. 421–447, 2001.

## Appendix C: Amplitude Effects

In Section 2, varying the fin wave amplitude around the condition at which the average horizontal force was zero showed no significant effect on the average horizontal force. At the time of publication, it was unclear why this was the case, because the existing literature generally accepts that amplitude changes do have a significant effect on thrust. However, further study into this phenomenon provided insight into why there was no significant effect apparent for that parametric study.

First, a different nominal flow speed was chosen for use with the same kinematics, in order to observe the effects when amplitude was perturbed around a point where a significant net thrust was already observed. For this study, the new nominal velocity was 0.4 m/s, which originally showed a net thrust of about 37 N/m for a maximum amplitude of 0.1 m. Figure C-1 shows the effect of varying amplitude about the nominal point. For this set of cases, amplitude does indeed show a significant effect on the average horizontal force, with a 70 N/m range over the same set of amplitudes as before. The RMS forces also increased in magnitude compared to the cases from Paper #1 by about 50%.

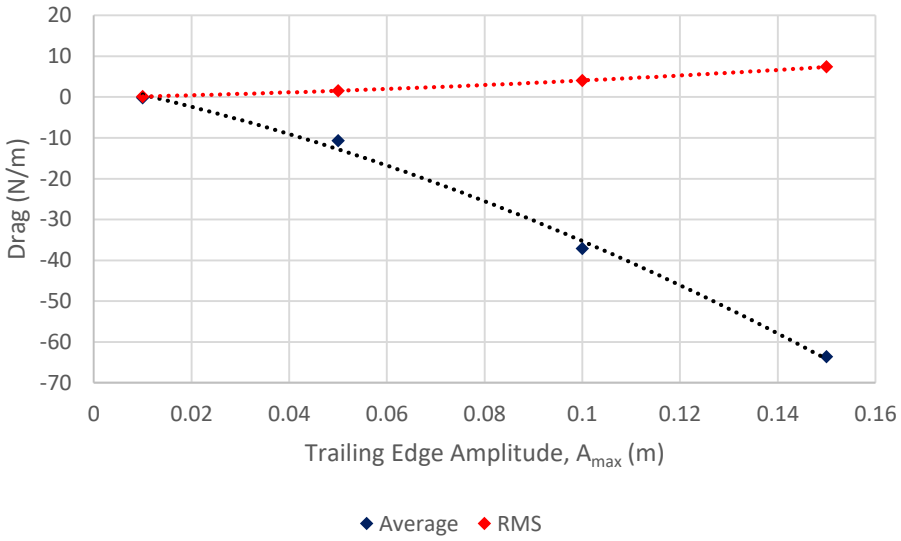


*Figure C-1: Average and RMS drag forces acting on the fin at different trailing edge amplitudes with conditions* $U_\infty = 0.4$, $f = 2.4\ Hz$, *and* $\lambda = 0.335\ m$.

The fact that amplitude did show an effect for the new cases begs the question as to why there was no effect before. To better understand the reasons why, one can examine the vorticity

in the wake region. The vorticity measures the rotation in the wake, and is useful for better understanding what kind of effect the fin had on the surrounding fluid. If the flow speed is faster than the wave speed, then the flow will dominate the wake, causing a von Karman vortex street to form, in which negative vortices form on the top half and positive vortices on the bottom, causing a suction region in between to drag the fin backward. If the wave speed is faster than the flow speed, the opposite will occur, and a jet will form down the centerline of the wake to propel the fin forward. Based on the results of Section 2, the wake can show symmetry when the flow speed is approximately equal to the wave speed, resulting in approximately zero average horizontal force.

Consider the vorticity in the wake for the following cases in Fig C-2. The original cases, where the wave speed is approximately equal to the swimming speed, show a vortex street where both positive and negative vortices each range from the top to the bottom of the wake, and are approximately vertically symmetric. Increasing the amplitude from 0.1 m to 0.15 m did increase the vertical length of those vortices as well as their magnitude, but did not change the overall flow structure. In other words, the wave speed and swimming speed balance each other out for these nominal cases, and while changing the amplitude of motion changes the wake, it does not affect the overall balance. For the 0.4 m/s cases, however, there was not vertical symmetry between the positive and negative vortices, and the positive vortices tended to lie above the centerline of the wake, and the negative vortices tended to lie below. When the amplitude increased, the wake increased in kind, amplifying the asymmetry in the wake. This interaction between wake symmetry and amplitude is ultimately at the root of the problem: when the effects of the fin and flow speed on the flow balance each other out, changes in trailing edge amplitude will preserve this balance.

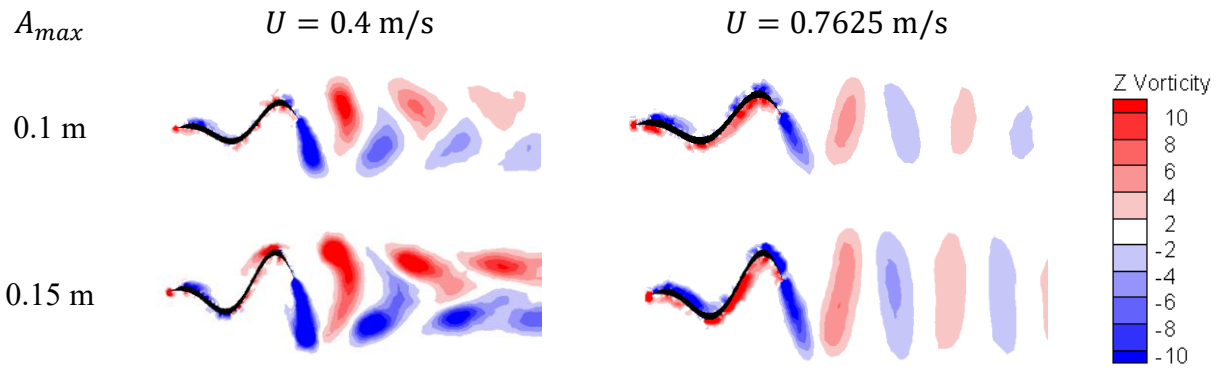


*Figure C-2: Vorticity contours in the wake of the fin motion for a swimming speed of 0.4 and 0.7625 m/s, with a trailing edge amplitude of 0.1 and 0.15 m.*

The reason this phenomenon may just now be coming to light is that the large majority of robotic and CFD studies of undulatory fin mechanics use a nonzero leading edge amplitude. When the leading edge is allowed to be nonzero, changes in amplitude of the fin wave will affect the leading edge vortex on the fin, causing changes in the perceived thrust. Holding the leading edge fixed prevents the leading edge vortex from forming, allowing one to examine the effects of the trailing edge amplitude alone. In practice, most fish do move the leading edge, but if those

oscillations at the leading edge are small or difficult to control, then it may be more useful to consider the added-mass effects controlled by the trailing edge motion. For fish using primarily the added-mass effect for propulsion, they would likely not be able to use amplitude to modulate swimming speed, as was the case here. Instead, they may modify the fin wavespeed to control the swimming speed, with amplitude changes limited to increasing the potential acceleration but not the swimming speed itself. In fact, Akanyeti et al [1] observed that in more than fifty species of fish, tail beat amplitude was significantly higher during acceleration than during steady swimming. Although this may not be the only factor at play, the phenomenon observed here may explain why fish use the trailing edge amplitude more for acceleration than for modulating swimming speed, and why robot designs may want to do the same.

[1] O. Akanyeti, Y. R. Yanagitsuru, W. J. Stewart, G. V. Lauder, and J. C. Liao, “Undulatory fishes increase tail beat amplitude during acceleration for high propulsive efficiency,” in *SICB 2017 Annual Meeting*, 2017.

**Appendix D: Free Body Diagram of the Simulated 2D Fin**

During simulation, the 2D fin experiences two types of forces: pressure and shear. The pressure forces act normal to the surface of the fin, while the shear forces act parallel to the fin surface. Both act along the length of the fin, as shown in the thrust-producing case of Figure D-1. The shear forces are approximately constant in magnitude along the length of the fin. However, the pressure forces vary considerably, with low pressure pockets on the front $(-x)$ edge of the wave and high pressure pockets on the rear $(+x)$ edge.

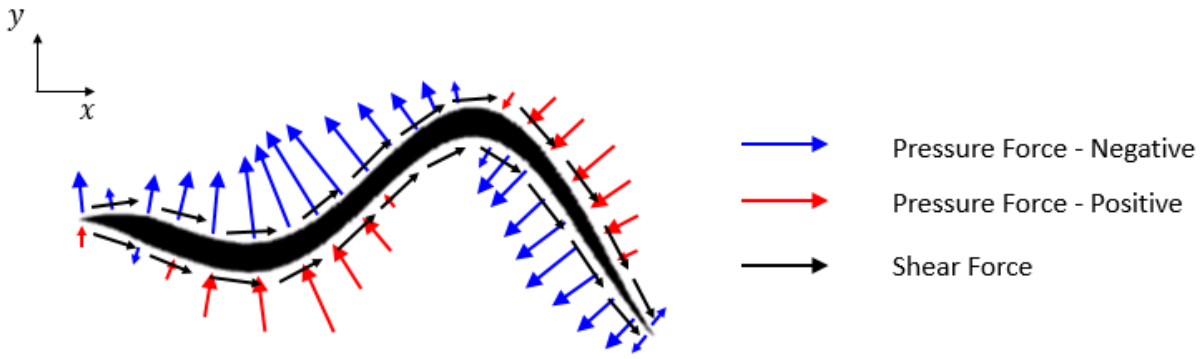


*Figure D-1: Fluid forces acting on the fin during a dynamic simulation in a case of net thrust.*

The CFD results yield pressure and shear forces for each node of the discretized mesh along the surface of the fin. Based on the angle of the differential element relative to the coordinate axes, these forces can then be separated into $x$ and $y$ components. In this way, each differential element has a net horizontal force $f_x$ and vertical force $f_y$. The moment $m_z$ is calculated from these forces about the center of gravity (CG) of the fin, at $x = L/2$ from the leading edge. The total forces and moment for the fin can then be calculated as:

$$F_x = \sum f_x \quad (1)$$

$$F_y = \sum f_y \quad (2)$$

$$M_z = \sum m_z \quad (3)$$

where the summation occurs over all nodes on the surface of the fin. Figure D-2 shows the net forces and moment acting on the fin at the CG for the case above. For this particular case, the net horizontal force was in the $-x$ direction, indicating net thrust, the net vertical force was in the $+y$ direction, and the net moment was in the $-z$ direction.

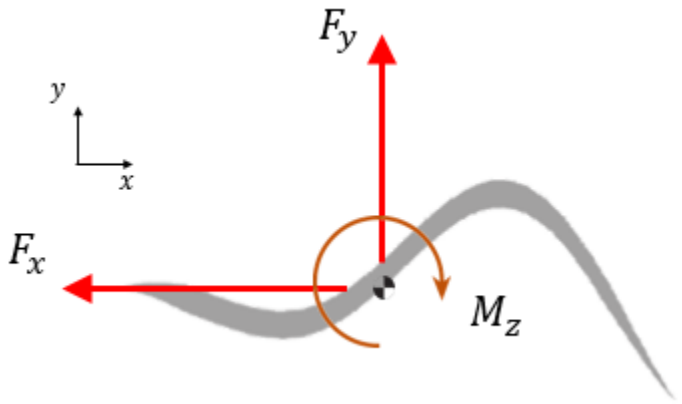


*Figure D-2: Net forces acting on the fin at a particular instant in time for a case of net thrust.*

Over the course of a full dynamic simulation, the net forces change in time. Once converged, the forces and moments vary approximately periodically. To quantify the unsteady effects of the fin motion, both the average and root mean square (RMS) forces were considered for analysis.